Experimental characterization of cohesive zone models for thin adhesive layers loaded in mode I, mode II, and mixed-mode I/II by the use of a direct method

G. Lélias[a,b], E. Paroissien[a], F. Lachaud[a,*], J. Morlier[a]

[a] Institut Clément Ader (ICA), Université de Toulouse, UPS, INSA, ISAE-SUPAERO, MINES-ALBI, CNRS, 3 rue Caroline Aigle, Toulouse 31400, France
[b] Sogeti High Tech, Aeropark, 3 Chemin Laporte, Toulouse 31300, France

Keywords:
Adhesively bonded joint
Cohesive zone model
Macro-element
Mode I
Mode II
Mixed-mode I/II
Singular value decomposition
Digital image correlation technique

A B S T R A C T

The demand for designing lightweight structures without any loss of strength or stiffness has conducted many engineers and researchers to seek for alternative joining methods. In this context, adhesive bonding may appear as an attractive joining method. However the interest of adhesive bonding remains while the structural integrity of the joint is ensured. According to recent literature the cohesive zone model (CZM) appears as a suitable approach able to predict both static and fatigue strength of adhesively bonded joints. This approach of the fracture process of adhesive layers is based on the modeling of the adhesive mechanical behavior through a set of adhesive cohesive properties in either mode I, mode II or mixed-mode I/II. The strength prediction of adhesively bonded joints is then highly dependent on the CZM parameters. The methods used to experimentally characterize them are thus essential. A new methodology, termed direct method, is presented and tested. It is based on the measurement of displacement field of bonded adherends at the crack tip of classical specimens allowing for the loading of the adhesive layer in pure mode I, pure mode II and mixed-mode I/II. The tested adhesive is a methacrylate–based two-component adhesive paste found under the reference SAF30 MIB manufactured by AEC Polymers (ARKEMA group). The adherends are in aluminium 6060. It is shown that it is possible to characterize the cohesive properties of the adhesive layer using the direct method. The numerical tests involve both adherends and adhesive nonlinearities. Nevertheless, the presented experimental implementation passes by the development of a dedicated data pre-processing to interpret the experimental measurements, highlighting the significance of the choice of the measurement means linked to the design of specimen.

1. Introduction

In the frame of structural design, the choice of joining technologies is decisive since they guarantee the integrity of the manufactured system. The mechanical fastening, such as riveting or screwing, appears the reliable solution for the designers. Nevertheless alone or in combination with the mechanical fastening, the adhesive bonding joining technology may offer significantly improved mechanical performance in terms of stiffness, static strength and fatigue strength (Hart-Smith, 1980; Kelly, 2006). The use of this higher level of mechanical performance allows for the design of lighter joints. In other words, the adhesive bonding offers the possibility to reduce the structural mass while ensuring the mechanical strength. The optimization of the strength-to-mass ratio is a challenge for several industrial sectors, such as aerospace, automotive, rail or naval transport industries. But, the reduction of structural mass makes sense only if the structural integrity is ensured. As result to take benefit from the adhesive bonding in view of mass reduction, it is required to be able to predict the strength of bonded joints. The strength prediction consists in the comparison of computed strength criteria to design allowable value. The strength criteria could be based on theoretical, empirical, semi-empirical investigations and possibly including in-service feedback. The stress analysis allows for the computation of input data, mandatory to the assessment of strength criteria. The experimental characterization allows then for the definition of design allowable value as well as of mechanical behavior to be used as input data of the mechanical analysis. As highlighted in (Jumel and al., 2013), the strength of a same joining system at macroscale depends on the experimental test specimen and procedure used, which contributes in restricted reliability or in extensive and expensive experimental

* Corresponding author.
E-mail address: eric.paroissien@isae-supaero.fr (E. Paroissien).

Nomencalture and units

BBe	bonded-beams element
CZM	cohesive zone model
DIC	digital image correlation
DoE	design of experiments
DCB	double cantilever beam
ENF	end notched flexure
FE	finite element
ME	macro-element
MMB	mixed mode bending
OSRA	optimal sub rank approximation
SLJ	single-lap joint
SVD	singular value decomposition
A_j	extensional stiffness (N) of adherend j
B_j	extensional and bending coupling stiffness (N mm) of adherend j
D_j	bending stiffness (N mm^2) of adherend j
E	adherend Young's modulus (MPa)
G_I	strain energy release rate (energy per unit of area: mJ or N/mm) in peel
G_{II}	strain energy release rate (energy per unit of area: mJ or N/mm)in shear
G_{Ic}	critical strain energy release rate (energy per unit of area: mJ or N/mm)in peel
G_{Ie}	adhesive elastic strain energy stored (energy per unit of area: mJ or N/mm)in peel
G_{IIc}	critical strain energy release rate (energy per unit of area: mJ or N/mm)in shear
G_{IIe}	adhesive elastic strain energy stored (energy per unit of area: mJ or N/mm)in shear
H	magnitude of applied displacement (mm)
J	J-integral parameter
K_{BBe}	elementary stiffness matrix of a bonded-beam element
L	length (mm) of bonded overlap
M_j	bending moment (N mm) in adherend j around the z direction
N_j	normal force (N) in adherend j in the x direction
P	magnitude of applied force (N)
S	adhesive peel stress (MPa)
S_{max}	maximal adhesive peel stress (MPa)
T	adhesive shear stress (MPa)
T_{max}	maximal adhesive shear stress (MPa)
V_j	shear force (N) in adherend j in the y direction
a	crack length (mm)
b	width (mm) of the adherends
d	damage parameter
e	thickness (mm) of the adhesive layer
h_j	half thickness (mm) of adherend j
k_I	adhesive elastic stiffness (MPa/mm) in peel
k_{II}	adhesive elastic stiffness (MPa/mm) in shear
n	power usd in the adhesive material law
n_ME	number of macro-elements
t	adherend thickness (mm)
u_j	displacement (mm) of adherend j in the x direction
v_j	displacement (mm) of adherend j in the y direction
Δ	overlap length (mm) of a macro-element
Δ_j	characteristic parameter of adherend j in N^2 mm^2
α	angle (rad) used for the definition the load application in MCB test
β	mixed-mode parameter
δ_t	numerical time step (s)
δ_u	displacement jump (mm) of the interface along the x-axis
δ_{ue}	displacement jump (mm) of the interface along the x-axis at initiation
δ_{uf}	displacement jump (mm) of the interface along the x-axis at propagation
δ_v	displacement jump (mm) of the interface along the y-axis
δ_{ve}	displacement jump (mm) of the interface along the x-axis at initiation
δ_{vf}	displacement jump (mm) of the interface along the x-axis at propagation
λ	norm of displacement jump (mm) of the interface
λ_e	norm of displacement jump (mm) of the interface at initiation
λ_f	norm of displacement jump (mm) of the interface at propagation
ν	adherend Poisson's ratio
θ_j	bending angle (rad) of the adherend j around the z direction

test campaign. According to (Li and al., 2006; Khoramishad et al., 2010, 2011; Da Silva and Campilho, 2012), the cohesive zone modeling – denoted CZM – appears as one of the most suitable approach able to model both the static and the fatigue behavior of adhesive joints. According to Khoramishad et al. (2010), the CZM have the advantage of: (i) considering finite strains and stresses at the adhesive crack tip, (ii) indicating both damage initiation and propagation as direct outputs of the model, (iii) advancing the crack tip as soon as the local energy release rate reaches its critical value with no need of complex moving mesh techniques. Based on Continuum Damage Mechanics and Fracture Mechanics, the CZM enables a diagnostic of the current state of the adhesive interface damage along the overlap. The damage, associated to micro-cracks and/or voids coalescence, results in a progressive degradation of the material stiffness before failure. An idealization of a CZM bilinear stress-strain relationship or CZM bilinear traction separation law is presented in Fig. 1. The CZM bilinear traction separation law is a well-established interface behavior that first assumes a linearly dependency relationship between the interface separation (deformation) and the resulting traction (stress). Once a prescribed value of separation is reached by the adhesive, the damage initiation is described in the form of a linearly decreasing resulting traction. Finally, the propagation of the damage is described by voluntarily fixing the resulting traction to zero, hence modeling the creation of two traction-free surfaces (i.e.: physical cracking). Both damage initiation and damage propagation phases are addressed in the model with no need of assuming any initial crack in the material (Valoroso and Champaney, 2004; De Moura et al., 2009; Campilho et al., 2013).

The strength prediction of adhesively bonded joints is then highly dependent on the CZM parameters. The methods used to experimentally characterize them are thus essential. As a result, numbers of authors have addressed this critical point over the past few years (Anderson and Stigh, 2004; Alfredsson et al., 2003, 2004; Leffler et al., 2007; Högberg, 2006; Högberg and Stigh, 2006; Cui et al., 2014; Azari et al., 2009; Gowrishankar et al., 2012; Wu et al., 2013). Most of these methods make use of the concept of the energetical balance associated to the computation of the path independent J-integral (Rice, 1968) along a closed contour of specifically designed joint specimens, known as the inverse method (Anderson and Stigh, 2004; Alfredsson et al., 2003, 2004; Leffler et al., 2007, Högberg, 2006; Högberg and Stigh, 2006). The inverse method is based on the energetical balance associated with the computation

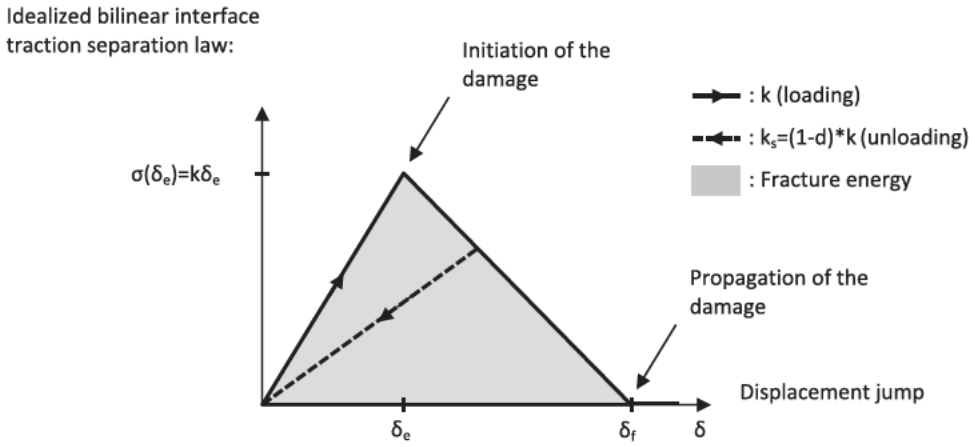

Fig. 1. Representation for an idealized bilinear interface traction separation law.

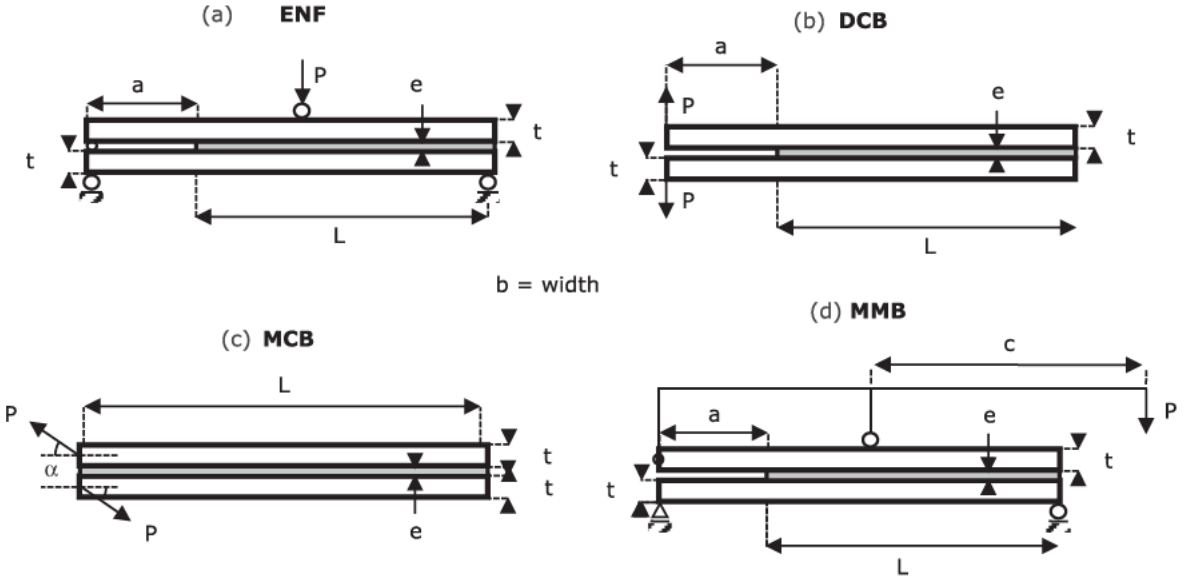

Fig. 2. Schematic representation for the (a) End notched flexure (ENF), (b) double cantilever beam (DCB) adhesive joint specimens. Idealized adhesive stress distributions, (c) mixed-mode cantilever beam (MCB) and (d) mixed-mode bending (MMB) adhesive joint specimens.

of the path independent J-integral (Rice, 1968) on a closed contour Γ:

$$J = \int W dy - \bar{T}\frac{d\bar{U}}{dx}ds \tag{1}$$

where W refers to the strain energy density, $\bar{T} = n\sigma$ to the traction vector, σ to the stress tensor, $\bar{U}$ to the displacement vector, n to the normal unit vector directed outward to the counter-clock wise integration path Γ, and (x,y) to the specified two-dimensional coordinate system. From the fundamental work by Fraisse and Schmit (1993) it is shown that the J-integral parameter can be computed from stress analysis based on a model of beam on an elastic foundation as:

$$J(\delta_u, \delta_v) = \int_0^{\delta_u} T(\delta_u, \delta_v)d\delta_u + \int_0^{\delta_v} S(\delta_u, \delta_v)d\delta_v \tag{2}$$

In the frame of the inverse method:

(I) the adhesive peel stress is obtained from experimental tests under pure mode I loading as (Anderson and Stigh, 2004):

$$S(\delta_v) = \frac{\partial J(\delta_u, \delta_v)}{\partial \delta_v} \tag{3}$$

(II) the adhesive shear stress is obtained from experimental tests under pure mode II loading as (Alfredsson et al., 2003):

$$T(\delta_u) = \frac{\partial J(\delta_u, \delta_v)}{\partial \delta_u} \tag{4}$$

(III) the adhesive peel and shear stresses are obtained from experimental tests under mixed-mode I/II loading as (Högberg, 2006; Högberg and Stigh, 2006):

$$S(\delta_v) = \frac{\partial J(\delta_u, \delta_v)}{\partial \delta_v} \tag{5}$$

$$T(\delta_u) = \frac{\partial J(\delta_u, \delta_v)}{\partial \delta_u} \tag{6}$$

The adhesive stresses are then derived from the J-integral. An advantage of this method is that it offers the possibility to monitor the evolution of the adhesive stress at the crack tip from the measurement of macroscopic quantities possibly measurable from experimental test fixtures, such as the applied load (in N) or the evolution of displacement jump (in mm) at the crack tip. Numbers of joint specimens have been explored for pure mode I, pure mode II and mixed-mode I/II characterization of adhesive layers. According to (Da Silva and Campilho, 2012), end notched flexure (ENF)

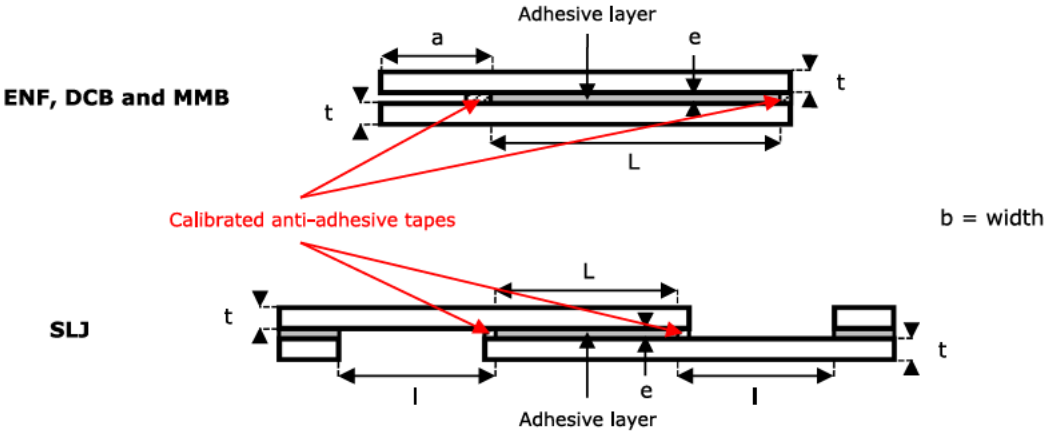

Fig. 3. Schematic representation for the manufacturing process of the ENF, DCB, MMB and SLJ joint specimens.

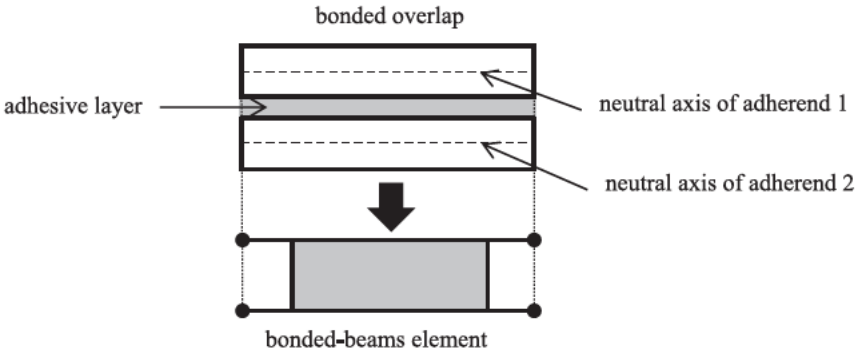

Fig. 4. Modelling of a bonded overlap by a bonded-beams element.

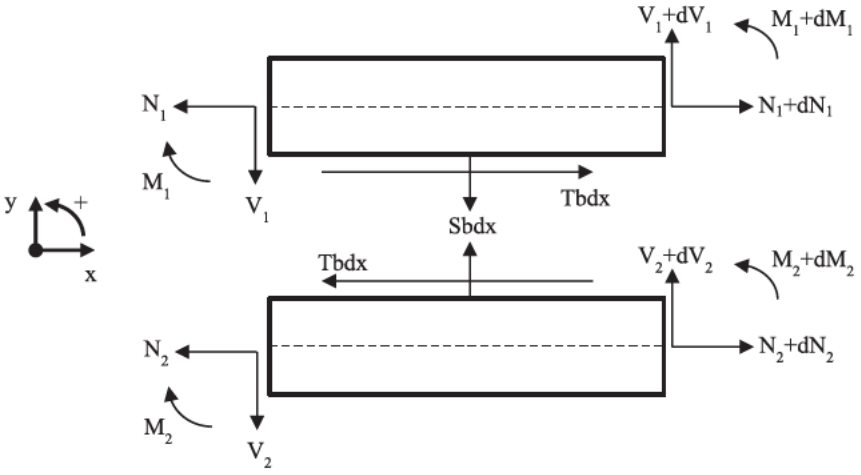

Fig. 5. Free body diagram of infinitesimal elements of the adherend 1 (top) and adherend (bottom).

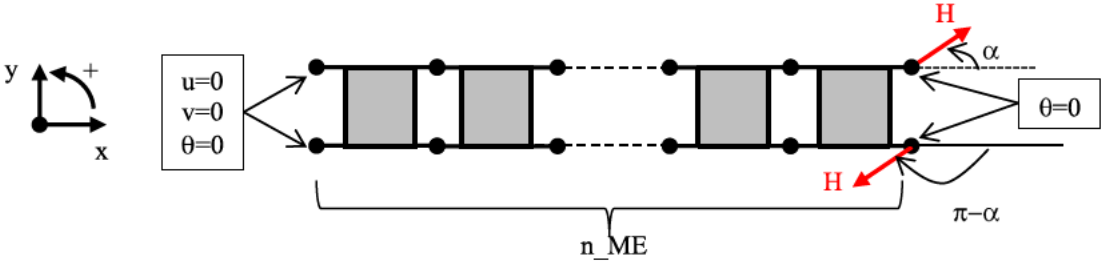

Fig. 6. Applied displacement H and fixed displacements for the MCB test configuration.

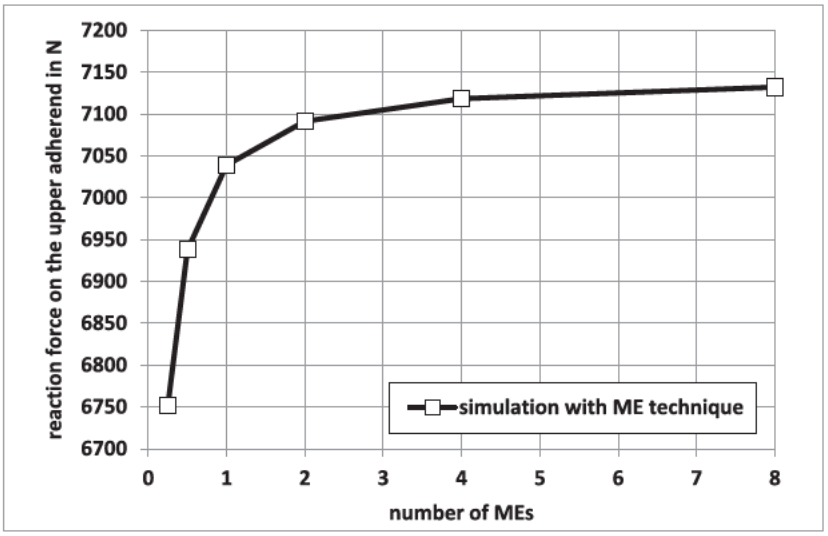

Fig. 7. Norm of the reaction force on the loaded section of the upper adherend.

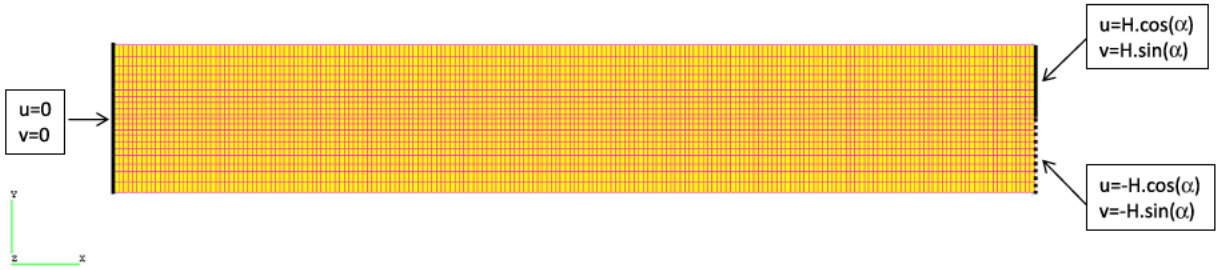

Fig. 8. View of the 3D FE model on the symmetry plane including the mesh (two MEs per mm) and the boundary conditions.

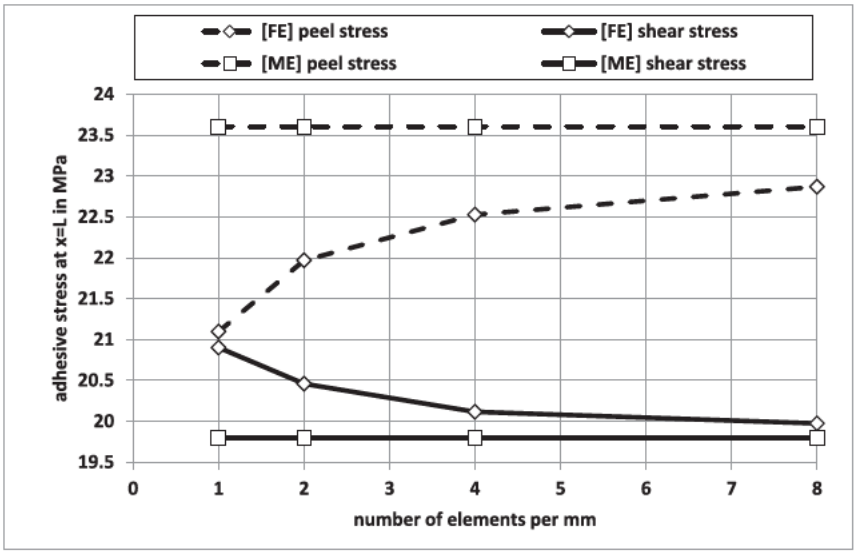

Fig. 9. Maximal peel and shear stresses at x = L reached during the run as a function of the mesh density for the FE and ME models.

and double cantilever beam (DCB) joint specimens have respectively emerged as the joint specimens the most frequently used for characterizing the cohesive properties of thin adhesive interfaces in pure mode I and pure mode II over the past years. An idealization of the linear elastic distributions of adhesive stresses (strains) resulting from the loading of both ENF and DCB joint specimens is presented in Fig. 2. According to (Reeder and Crews, 1990; Kenane and Benzeggagh, 1997; Högberg, 2006) most of the mixed-mode I/II test fixture present practical limitations: (i) complex loading fixtures, (ii) unstable fracture process, (iii) complex manufacturing of the test samples. However, both mixed mode cantilever beam (MCB) and mixed mode bending (MMB) joint specimens offer the possibility of working over a wide range of adhesive mixed-mode ratios without modifying the geometry (Fig. 2).

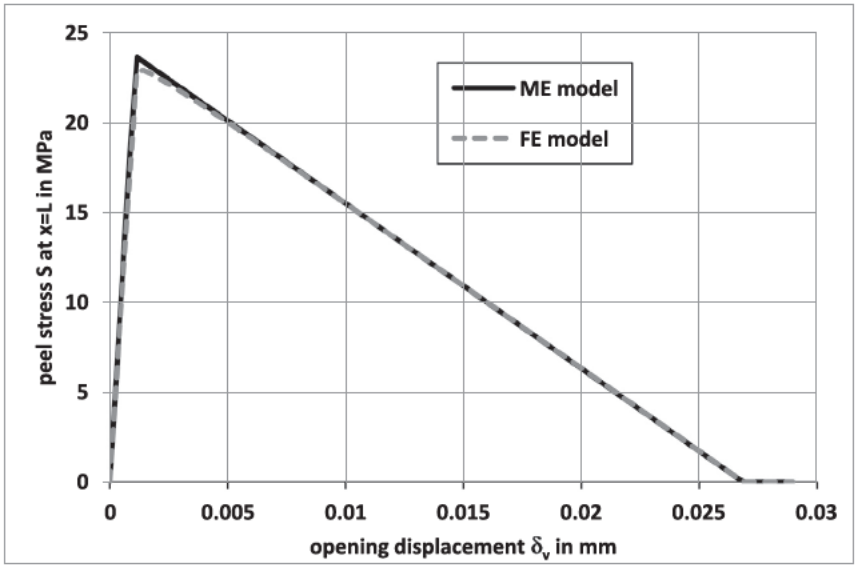

Fig. 10. Evolution of the adhesive peel stress as a function of the opening displacement at $x = L$ for the FE and ME models with a mesh density of eight elements per mm.

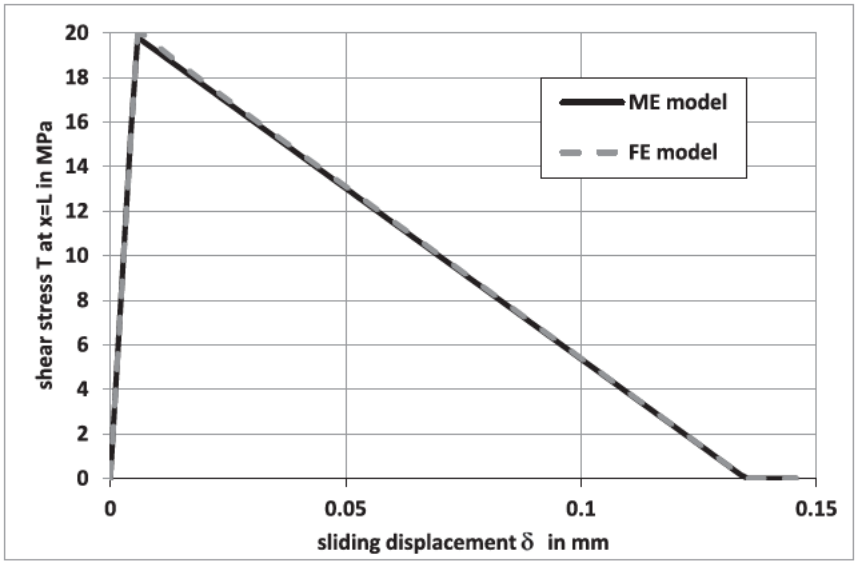

Fig. 11. Evolution of the adhesive shear stress as a function of the sliding displacement at $x = L$ for the FE and ME models with a mesh density of eight elements per mm.

However, the methods based on J-integral are valid only when the J-integral is valid. If the J-integral can be computed through a data reduction scheme based on a model of a beam on elastic foundations for the adhesive bonded overlap (Fraisse and Schmit, 1993), the J-integral is not suitable when the materials are dependent on time. Another restriction is the consideration of unloading phases within the loading history. Various types of CZM for mixed-mode exist in the literature (Goustanios and Sørensen, 2012). One widespread type is based on the definition of traction-separation laws in pure modes, which are coupled with interaction laws for damage initiation and damage propagation under mixed-mode. Goustanios and Sørensen show that the mixed-mode truss-like CZMs are path-dependent. The mixed-mode truss-like CZMs are a particular case of mixed-mode CZM based on the definition of pure modes laws linked by interaction laws under mixed-mode. If the J-integral is path-independent along the spatial integration path, it is shown that the J-integral, which is shown to be a potential function from which derive the cohesive stress, is dependent on the loading path history. A direct consequence for truss-like CZMs is thus that Eq. (2) does not imply Eqs. (5) and (6), so that the use of the inverse method should not be suitable to any type of CZM.

The objective of this paper is to suggest a direct method to assess CZMs for the modelling of adhesively bonded joints, overcoming the restrictions involved in methods based on J-integral. In the first part, the inverse method is employed on the results of a numerical test campaigns on MCB configuration. A mixed-mode CZM based on the definition of pure mode bilinear laws linked by interaction laws under mixed-mode is used for this test campaign in order to show the deviation of predictions obtained from the inverse method. The numerical analyses are performed using three-dimensional finite element (3D FE) model as well as the macro-element (ME) technique (Paroissien, 2006a; Paroissien et al., 2006b, 2007, 2013; Lélias et al., 2015). In the second part,

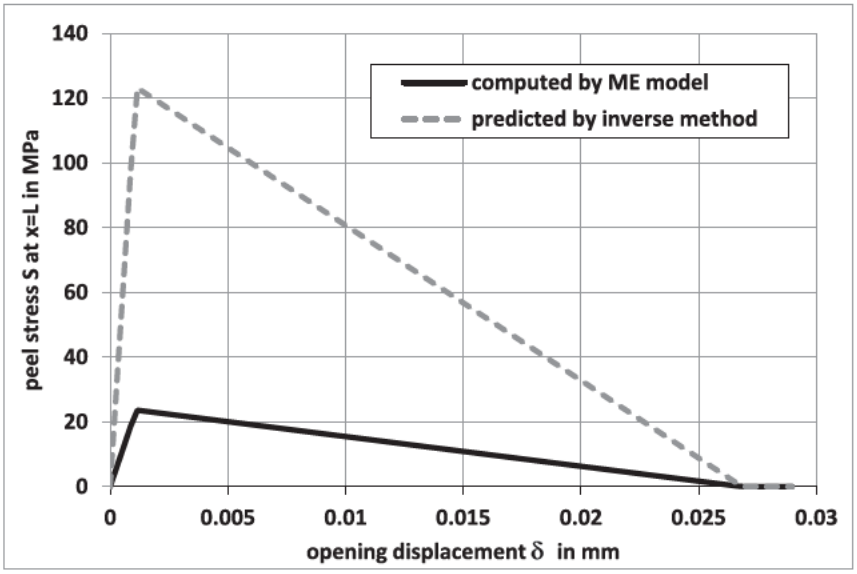

Fig. 12. Evolution of the adhesive peel stress as a function of the opening displacement at $x = L$ as computed by the ME model with a mesh density of eight elements per mm and predicted by the inverse method.

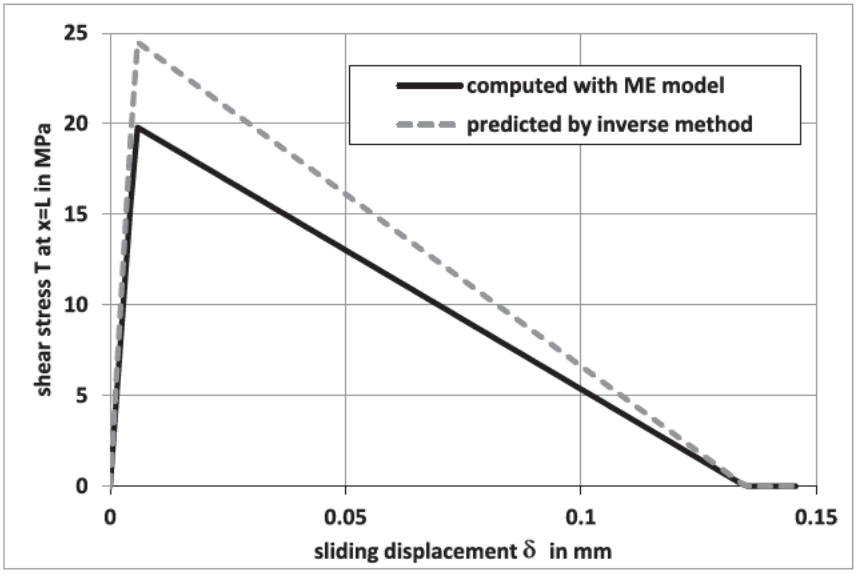

Fig. 13. Evolution of the adhesive shear stress as a function of the sliding displacement at $x = L$ as computed by the ME model with a mesh density of eight elements per mm and predicted by the inverse method.

an approach based on design of experiments (DoE) is presented to assess the main parameters affecting the experimental assessment of CZM. Finally, in the part, the direct method is applied to characterize the CZM properties in mode I, mode II and mixed-mode I/II through the use of double cantilever beam (DCB) specimen, end notched flexure (ENF) specimen and mixed mode bending (MMB) specimen, respectively (see Fig. 3). Finally the single-lap bonded joint (SLJ) configuration is used to assess the relevance of the method (see Fig. 3).

2. Numerical test campaign

2.1. Overview of the numerical test campaign

In the frame of the numerical test campaign presented in this paper, the MCB test configuration has been selected. It has been suggested by Högberg and Stigh (2006). Similarly to the DCB test configuration, the loading consists in a pair of forces (termed P), being of the same magnitude but in opposite directions. Nevertheless, the action direction of the pair of forces is defined by an angle α, which allows for the adhesive layer to be submitted to pure mode I, pure mode II and mixed-mode I/II (see Fig. 2). The selected specimen design, including geometrical and material parameters, corresponds to the one described by Högberg and Stigh (2006). The crack length $a = 0$ is then chosen. The geometrical parameters are provided in Table 1 in conjunction with Fig. 2. In this numerical test campaign, only one angle α is chosen $\alpha = \pi/16$.

Table 1
Geometrical parameters of the MCB specimen.

a in mm	b in mm	e in mm	t in mm	L in mm
0	4	0.2	8	100

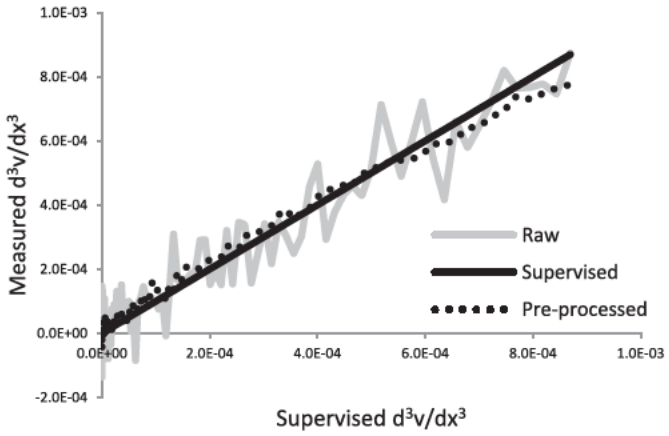

Fig. 14. Comparison of the 3rd order derivative of the deflection of the neutral fiber of the upper adherend obtained from raw and pre-processed experimental results.

The adherends are made of steel with a Young's modulus $E = 200\,\text{GPa}$ and a Poisson's ratio $\nu = 0.3$. The design is such that the adherends will remain in their linear elastic domain. The adhesive is assumed to have a classical bilinear damage evolution law following (Allix and Ladevèze, 1996), involving interaction energy laws for both initiation and propagation under mixed-mode:

$$\begin{cases} \left(\frac{G_I}{G_{Ie}}\right)^n + \left(\frac{G_{II}}{G_{IIe}}\right)^n = 1 \\ \left(\frac{G_I}{G_{Ic}}\right)^m + \left(\frac{G_{II}}{G_{IIc}}\right)^m = 1 \end{cases} \tag{7}$$

where $n = m$ is a material parameter to be identified, G_{Ic} and G_{IIc} are the critical strain energy release rate in mode I and mode II, G_{Ie} and G_{IIe} are the elastic strain energies stored in mode I and mode II and G_I and G_{II} are related to the strain energy release rates in mode I and mode II, respectively. For this numerical test campaign, $n = 1$ is chosen. The fracture energies in mode I and mode II and the elastic stiffnesses under peel and shear, termed k_I and k_{II} respectively are the same as those used by Högberg and Stigh, (2006). Nevertheless, the adhesive maximal peel and shear stresses, termed S_{max} and T_{max}, is different, to ensure a right energy dissipation during loading (Turon et al., 2010). It is indicated that the law by Allix and Ladevèze (1996) already includes this condition. It is then chosen to keep the same maximal shear stress $T_{max} = 26\,\text{MPa}$, resulting in a maximal peel stress $S_{max} = 36.6\,\text{MPa}$, instead of 20 MPa. The choice consisting in keeping S_{max} to its original value instead of T_{max} does not change qualitatively the results provided in his paper. The material parameters of the adhesive layer are given in Table 2. In the following, the 3D FE model and the ME model are presented. Then the results of the numerical test campaign are provided including those relating to the convergence study of numerical models. Finally, the direct method is described.

2.2. Macro-element model

2.2.1. Macro-element technique

The numerical analysis is performed using the ME technique for the modelling of bonded overlap (Paroissien, 2006a; Paroissien et al., 2006b, 2007, 2013; Lélias et al., 2015). The ME technique is inspired by the FE method and differs in the sense that the interpolation functions are not assumed, since they take the shape of the solutions of the governing differential equation system. A direct consequence is that only one ME is sufficient to mesh a complete bonded overlap in the frame of a linear stress analysis. The bonded overlap is then modelled by a four-node ME – also called bonded-beams element – the nodes of which are located at the extremities of the overlap on the neutral axes of adherends (see Fig. 4). This ME involves 3 degrees of freedom per node or a total of twelve for a 1D-beam analysis.

The main work is thus the formulation of the elementary stiffness matrix of the bonded-beams element. Indeed once the stiffness matrix of the complete structure is assembled from the elementary matrices and the boundary conditions are applied, the minimization of the potential energy provides the solution, in terms of distributions along the overlap of adhesives stresses, internal forces and displacements in the adherends. An approach for the formulation of the stiffness has already been described in detail in previous papers (Paroissien, 2006a; Paroissien et al., 2006b, 2007, 2013; Lélias et al., 2015). Nevertheless, this approach could be long to set up. In this paper, a new approach is provided in Appendix A for a fast and easy implementation within a mathematical software such as SCILAB for example. Compared with the early approach, the shape of solutions in terms of displacements and internal loads is not provided. Nevertheless, in the frame of nonlinear material analyses such as the one presented in this paper, the bonded overlap has to be meshed in order to locally update the material parameters within an iterative computation procedure. As a result, the displacements and internal loads are directly read at nodes. Moreover, the following description is useful for the derivation of the direct method.

2.2.2. Hypotheses

It is assumed that the thickness of the adhesive is constant along the length Δ of the macro-element. Moreover, the adherends are simulated as linear elastic Euler–Bernoulli laminated beams. The general shape of the constitutive equations for the adherend

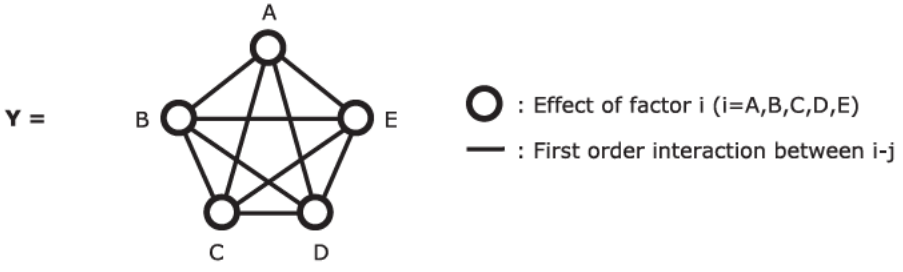

$$Y = M+E(A)+E(B)+E(C)+E(D)+E(E) +I(AB)+I(AC)+I(AD)+I(AE)+I(BC)+I(BD)+I(BE)+I(CD)+I(CE)+I(DE)$$

Fig. 15. Linear Taguchi's graph of main effects and interactions.

Table 2
Adhesive material parameters.

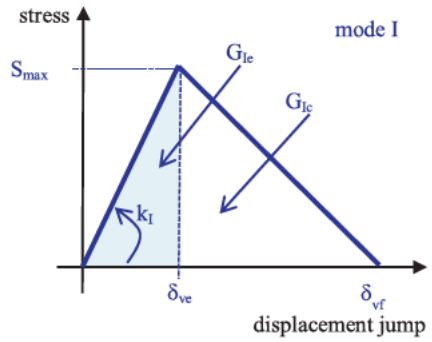

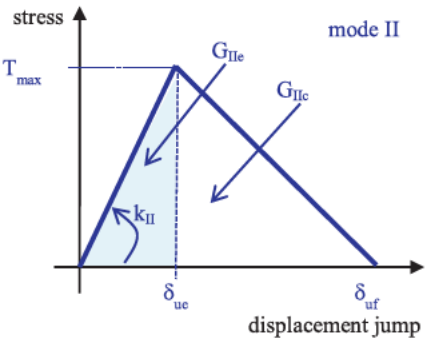

G_{Ic} in N/mm	G_{Ie} in N/mm	G_{IIe} in N/mm	G_{IIc} in N/mm
0.76	3.128 E−2	3.464 E−2	2.30
δ_{ve} in mm	δ_{vf} in mm	δ_{ue} in mm	δ_{uf} in mm
1.71 E−3	4.15 E−2	7.28 E-3	1.77 E−1
k_I in GPa/mm	S_{max} in MPa	k_{II} in GPa/mm	T_{max} in MPa
21.4	36.6	3.57	26

$j = 1,2$ provides the six first differential equations:

$$\begin{cases} N_j = A_j\frac{du_j}{dx} - B_j\frac{d\theta_j}{dx} \\ M_j = -B_j\frac{du_j}{dx} + D_j\frac{d\theta_j}{dx} \\ \theta_j = \frac{dv_j}{dx} \end{cases} \Leftrightarrow \begin{cases} \frac{du_j}{dx} = \frac{D_j}{\Delta_j}N_j + \frac{B_j}{\Delta_j}M_j \\ \frac{dv_j}{dx} = \theta_j \\ \frac{d\theta_j}{dx} = \frac{B_j}{\Delta_j}N_j + \frac{A_j}{\Delta_j}M_j \end{cases} \quad (8)$$

where N_j (M_j) is the normal force (bending moment) of the adherend j and u_j (v_j, θ_j) is the longitudinal displacement (deflection, bending angle) of the adherend j. For the adherend j, A_j represents the extensional stiffness, D_j the bending stiffness and B_j the coupling stiffness and $\Delta_j = A_jD_j - B_jB_j \neq 0$ (see Appendix C).

The adhesive layer is simulated by an infinite number of elastic shear and transverse springs attached at both adherend interfaces. The adhesive shear stress – denoted T – and the adhesive peeling stress – denoted S – are then given by:

$$\begin{cases} S = k_I(v_1 - v_2) \\ T = k_{II}(u_2 - u_1 - h_2\theta_2 - h_1\theta_1) \end{cases} \quad (9)$$

where h_j is the half thickness of adherend j. In this paper, $h_1 = h_2 = t/2$.

The classical local equilibrium from Goland and Reissner (1944) is used and provides the six last differential equations for $j = 1,2$ (see Fig. 5):

$$\begin{cases} \frac{dN_j}{dx} = (-1)^j bT \\ \frac{dV_j}{dx} = (-1)^{j+1} bS \\ \frac{dM_j}{dx} + V_j + bh_jT = 0 \end{cases} \quad (10)$$

where V_j is the shear force of the adherend j.

2.2.3. Non linear computation

The use of a nonlinear adhesive material implies that the computation is nonlinear. A detailed description of the nonlinear algorithm used is provided in Lélias et al. (2015). Only a brief overview is given here. The algorithm is based on Newton-Raphson and uses the secant stiffness matrix with an update at each iteration. In particular, the damage parameter is computed at each nodal abscissa according to the introduced adhesive material law. The norm of displacement jump (in mm) of interface λ is defined by:

$$\lambda = \sqrt{(\delta_v)^2 + (\delta_u)^2} \quad (11)$$

where δ_v (δ_u) is the displacement jump of the interface (see Table 2) along the y-axis (x-axis). A mixity parameter β is defined by:

$$\beta = \frac{\delta_u}{\delta_v} = \frac{u_2 - u_1 - h_2\theta_2 - h_1\theta_1}{v_1 - v_2} \quad (12)$$

At each iteration, the mixity parameter β is updated. Under the current local mixity parameter, it assumed that the material law is bilinear, so that the damage parameter d is such that:

$$d = \frac{\lambda_f(\lambda - \lambda_e)}{\lambda(\lambda_f - \lambda_e)} \quad (13)$$

where λ_e (λ_f) is the displacement jump (in mm) of the interface at initiation (propagation). In order to compute λ_e (λ_f), the interaction laws Eq. (1) are used while classically assuming that the projections on pure modes of the mixed mode evolution law under the current local mixity are bilinear (see Table 2):

$$\begin{cases} \lambda_e = \delta_{ue}\delta_{ve}\sqrt{1+\beta^2}\left[\frac{1}{(\delta_{ue})^{2n} + (\beta\delta_{ve})^{2n}}\right]^{\frac{1}{2n}} \\ \lambda_f = \delta_{uf}\delta_{vf}\sqrt{1+\beta^2}\left[\frac{\sqrt{(\delta_{ue})^{2n} + (\beta\delta_{ve})^{2n}}}{(\delta_{ue}\delta_{uf})^n + (\beta^2\delta_{ve}\delta_{vf})^n}\right]^{\frac{1}{n}} \end{cases} \quad (14)$$

The damage parameter is computed only if δ_v is positive. Each ME is then updated with the damaged elastic stiffness taken as the maximal value of both damage parameters computed at each extremity of the ME.

Finally, the displacement is linearly applied as a function of the numerical time. Each numerical test result is obtained from a simulation run involving one hundred constant time steps δ_t.

2.2.4. Mesh and boundary conditions

The bonded overlap is regularly meshed with a parametrical number *n_ME* of bonded-beams elements. One extremity is clamped and the loading is applied under displacement (termed H) at the other extremity where the bending angle is fixed (see Fig. 6). The applied displacement is $H = 0.074$ mm so that the damage begins to propagate in the adhesive layer at the loaded extremity. In view of the application of the inverse method, it is mandatory that the adhesive layer does not deform at the joint extremity where the load is not applied. Clamping conditions avoid both peel and shear deformations.

The results are not presented in this paper but a study on the influence of mesh size up to a maximal mesh density of twenty

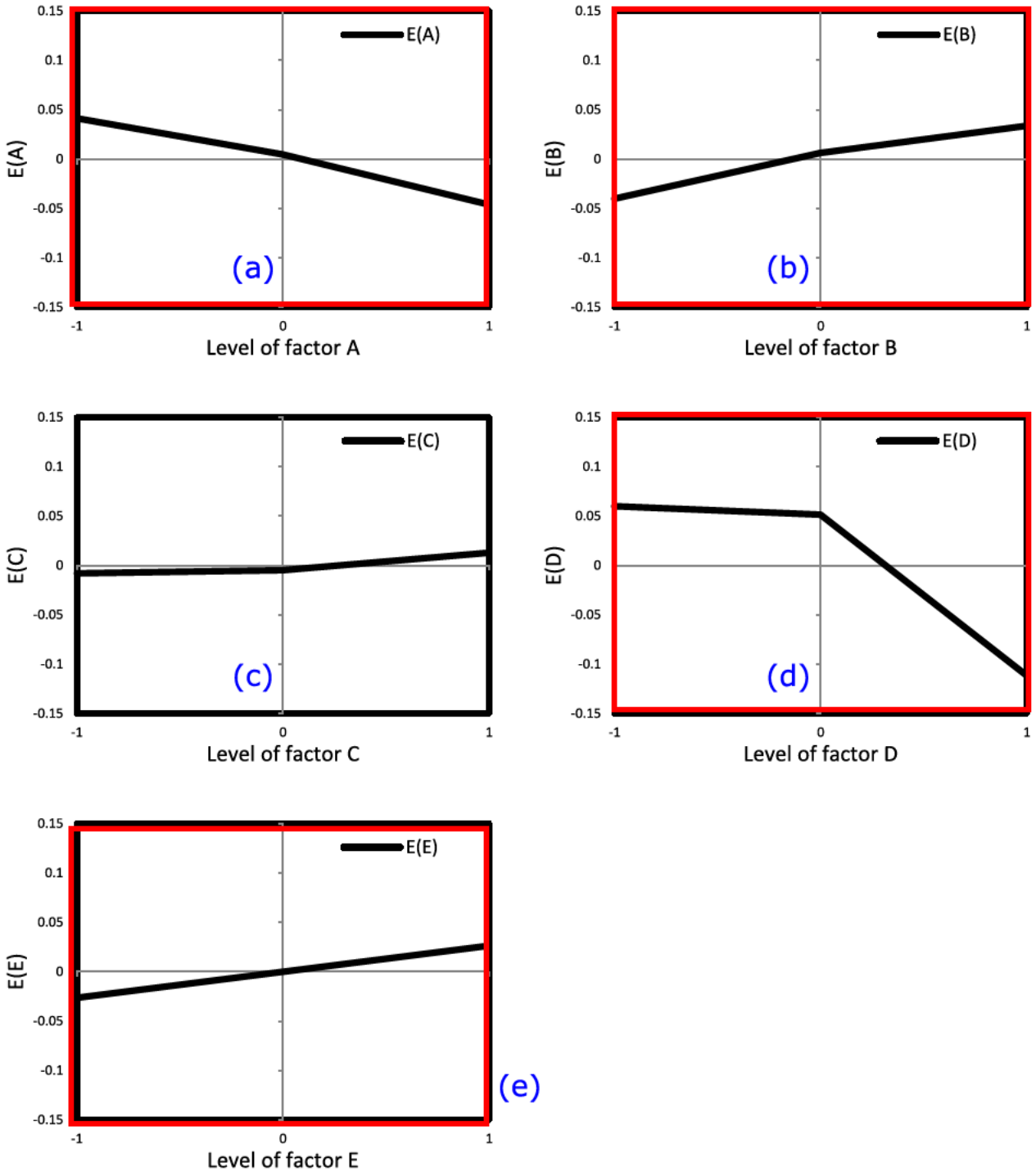

Fig. 16. Effect of factor i ($i = A,B,C,D,E$) on the correlation coefficient r^2. Influence of the experimental (algorithmic) parameters on the accuracy of the experimental measures. Red = Significant effects. Black = Negligible effects. (For interpretation of the references to color in this figure legend, the reader is referred to the web version of this article.)

ME per mm was performed under a pure linear elastic analysis under pure mode I ($\alpha = \pi/2$). The conclusions are that (i) the original approach and the present approach (see Appendix A) for the formulation of the elementary stiffness matrix of ME provides exactly the same results, and (ii) the computed reaction as well as the adhesive peak stresses do not vary at all with the mesh density.

2.2.5. Results

In order to assess the influence of the mesh density on the predictions from the ME model, four runs associated with the four following mesh densities are launched: (i) one ME per mm, (ii) two MEs per mm, (iii) four MEs per mm and (iv) eight MEs per mm. The norm of the reaction force on the loaded section of the upper adherend as a function of the mesh density is provided in Fig. 7. It is shown that the model converges when the mesh density is increased. Moreover, the maximal peel and shear stresses at $x = L$ reached during the runs are constant when the mesh density varies and equal to: $S_{max} = 23.6$ MPa and $T_{max} = 19.8$ MPa. This result is not surprising since the load is applied under the shape of displacement at the location where the adhesive stress evolution is

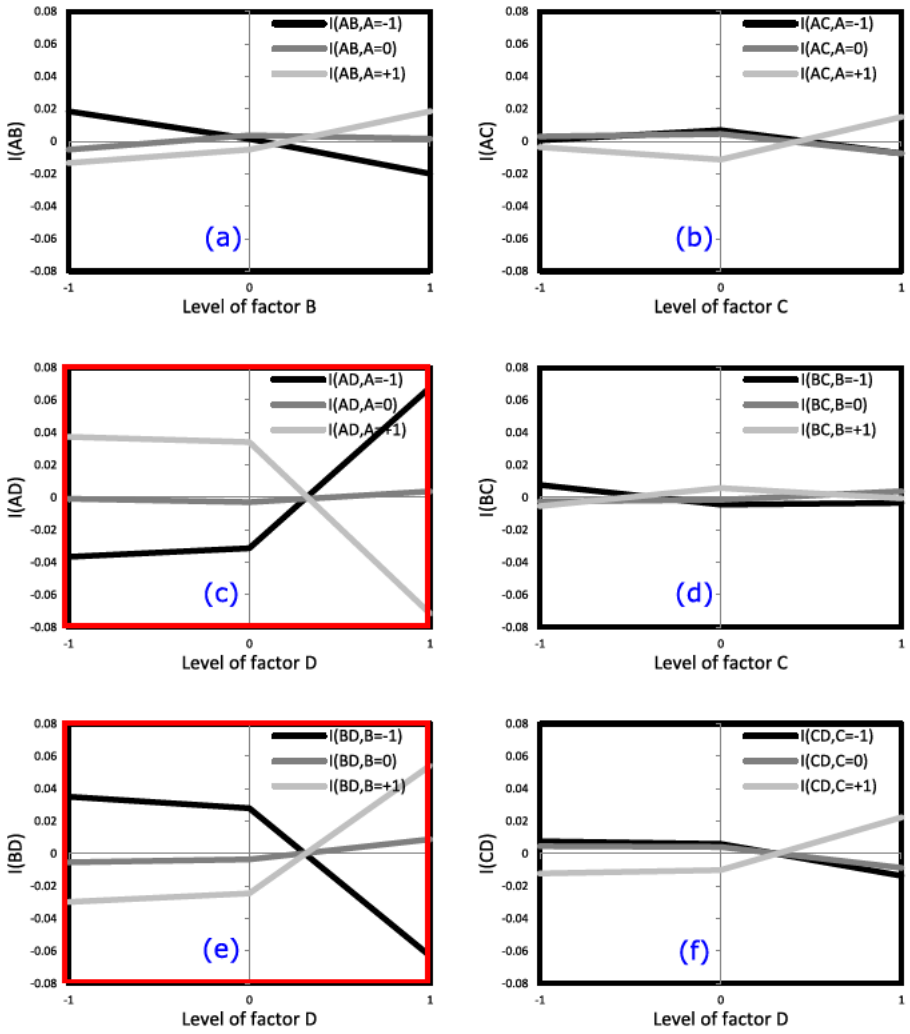

Fig. 17. First order interaction between factors *i-j* ($i,j = A,B,C,D,E$) on the correlation coefficient r^2. Influence of the experimental (algorithmic) parameters on the accuracy of the experimental measures. Red = Significant interactions. Black = Negligible interactions. (For interpretation of the references to color in this figure legend, the reader is referred to the web version of this article.)

observed and the stiffness matrix is updated considering the maximal value of both damage parameters computed at each extremity of the ME.

2.3. Finite element model

2.3.1. Mesh and boundary conditions

A 3D FE model is developed using the FE code SAMCEF v18.1 (LMS PLM software). This model makes use of linear brick elements with eight nodes and twenty-four degrees of freedom for the adherends. A normal integration rule is selected. The adherends are assumed linear elastic. The adhesive layer is simulated through 3D quadrangular interface elements. The CZM defined in Section 2.1 is applied through the Damage Interface SAMCEF material. The adhesive layer is regularly meshed along the overlap length and width, with a constant aspect ratio equal to one: all the interface elements are squared. The adherends mesh is coincident at the interface with the adhesive layer. The mesh along the thickness of adherends is distributed as it follows. The adherends are cut at their own neutral plane in two parts. A distributed mesh is applied on each part and a transition ratio equal to one is applied at the neutral plane. The size along the thickness of the last element at the neutral axis of the adherend is fifty percent larger than those of the first element at the interface with the adhesive layer. The same size ratio is applied for the second part. The mesh of two adherend parts at the neutral plane is then coincident, so that a kinematic bonding of nodes is applied. As a result, following the previous meshing method, the number of elements along the overlap drives the meshing of the full model. The boundary conditions are relevant to those applied in the previous ME model. Only one half of specimen is modelled and symmetry conditions are applied. The adherends are clamped at one extremity and loaded under displacement at the other extremity (see Fig. 8). It is indicated that the boundary conditions applied on the FE element model are relevant to those applied on the ME model. In particular, at the loaded extremity, the longitudinal displacement at the interface with the adhesive layer is the one at the neutral axis.

2.3.2. Nonlinear computation

The nonlinear computation is based on a Newton Raphson scheme, for which the stiffness matrix is updated at each iteration with the secant properties concerning the adhesive layer. The computation remains geometric linear, due the level of displacements and rotation. The applied displacement is $H = 0.074$ mm as for the simulations based on ME model. It is sufficient to apply the inverse method. As for the simulations based on the ME model, each numerical test result is obtained from a simulation run involving one hundred constant time steps δ_t.

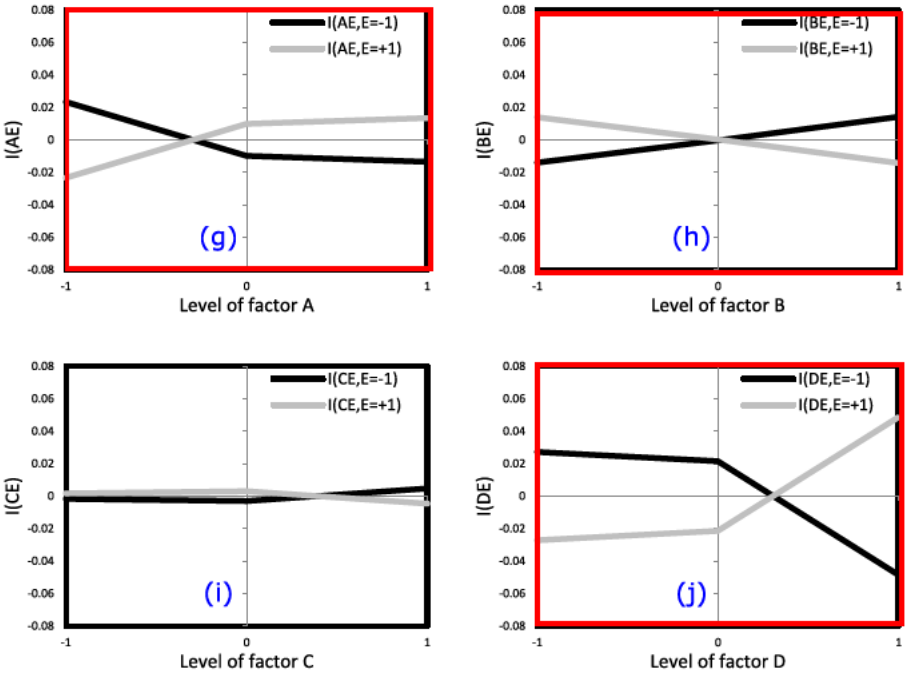

Fig. 17. Continued

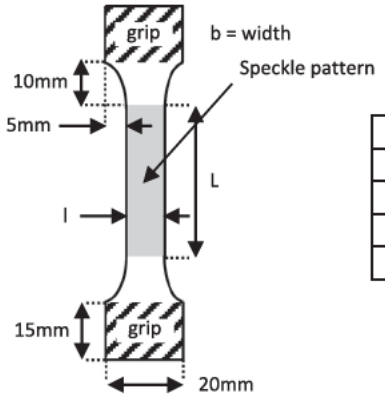

	b	l	L
TT_1	3.95mm	9.96mm	60mm
TT_2	3.95mm	9.95mm	60mm
TT_3	3.94mm	9.95mm	60mm
TT_4	3.96mm	9.96mm	60mm

Fig. 18. Geometry of the aluminum bulk specimens.

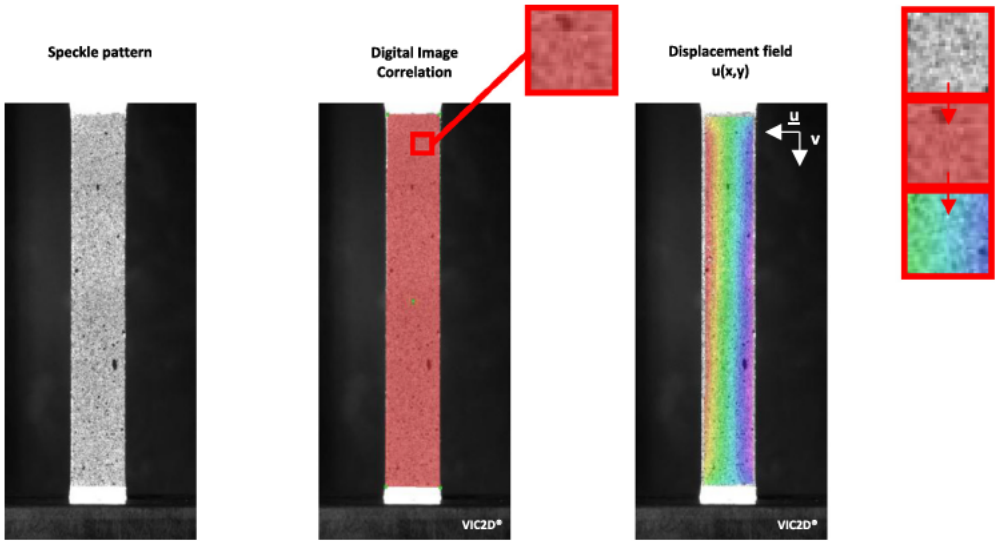

Fig. 19. Measuring the displacement field of aluminum bulk specimens using digital image correlation (DIC) techniques.

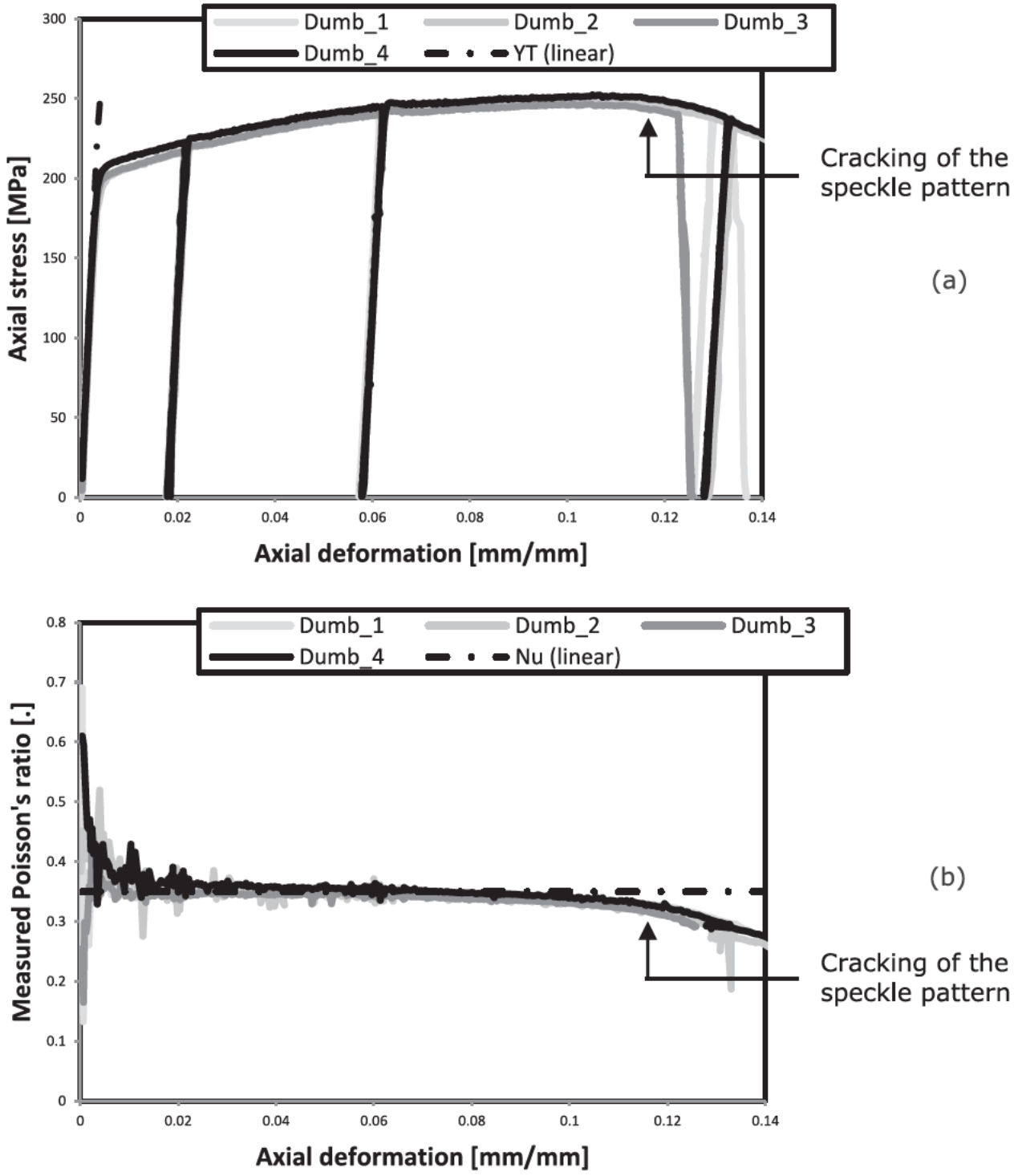

Fig. 20. Experimental characterization for aluminum bulk specimens in terms of axial stress-strain evolution law (a) and evolution of the measured Poisson's ratio (b). YT is the Young's modulus.

2.3.3. Results

As for the ME model, the influence of the mesh density on the predictions from the FE model is assessed using the same 4 mesh densities. The maximal peel and shear stresses at $x=L$ reached during the run is provided in Fig. 9 as a function of the mesh density. It is shown that these adhesive peak stresses converges when the mesh density is increased, while tending to the adhesive peak stresses predicted by the ME model. For a mesh density of eight element per mm, the relative difference in the FE model prediction from the ME model prediction is −3.11% in peak peel stress and +0.90% in peak shear stress. The evolution of the adhesive peel (shear) stress as a function of the opening (sliding) displacement at $x=L$ for the FE and ME models with a mesh density of eight elements per mm is provided in Figs. 10 and 11. A very good agreement is then shown between the predictions of the FE and ME models.

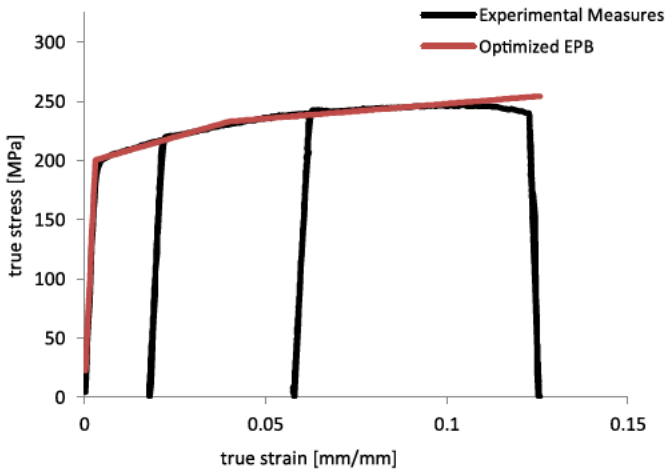

Fig. 21. Experimental characterization of aluminum bulk specimens. Representation for the optimized trilinear elastic plastic stress-strain evolution law.

2.4. Application of the inverse method

The inverse method is applied on the predictions of the ME model with a mesh density of eight element per mm.

Firstly, the J-integral parameter at $x=L$ has to be computed according to Eq. (2). Taking benefit from the elevated number of computation time, a simple numerical integration is then performed as:

$$J(t_f)=\sum_{i=1}^{i=f}T(t_i)[\delta_u(t_i)-\delta_u(t_{i-1})]+\sum_{i=1}^{i=f}S(t_i)[\delta_v(t_i)-\delta_v(t_{i-1})] \tag{15}$$

where t_i is the ith computation time, t_f is the las computation time and t_0 is equal to zero. It is indicated that this computation of the J-integral is valid in the abscissa $x=L$ only and at any time, because (i) the applied loading on the neutral line in terms of δ_u and δ_v is the same as the one seen at the interface in $x=L$ ($\theta=0$) and (ii) the applied loading is proportional at any time. As a result, the mixed mode parameter β is constant at any time in $x=L$ and the shear (peel) stress is only dependent on δ_u (δ_v) at the given constant β.

Secondly, the adhesive stresses are computed according to Eqs. (5) and (6). The required differentiation of the J-integral parameter is obtained by taken the slope between two consecutive times:

$$\begin{cases} S(\delta_v(t))=\frac{J(t)-J(t-\delta_t)}{\delta_v(t)-\delta_v(t-\delta_t)} \\ T(\delta_u(t))=\frac{J(t)-J(t-\delta_t)}{\delta_u(t)-\delta_u(t-\delta_t)} \end{cases} \tag{16}$$

The evolution of the adhesive peel (shear) stress as a function of the opening (sliding) displacement at $x=L$ as computed by the ME model with a mesh density of eight elements per mm and predicted by the inverse method is provided in Figs. 12 and 13. It is shown that the predictions of the inverse method does not fit those of the ME models. It is then concluded that the considered CZM is an example for which the inverse method fails to predict the adhesive peel and shear stresses under mixed-mode. This example is not a general proof for this type of CZM. However, the main fact is that the application of the inverse method associated with particular types of CZM could lead to incorrect behavior assessment.

2.5. Description of the direct method

This method is presented in (Lélias, 2016). It is based on the measurement around the crack tip of the displacement of the neutral axis according to the x-axis and the y-axis. Contrary to the inverse method, no spatial integration of equilibrium equations is required.

In the case of pure mode I loading, the adhesive shear stress vanishes so that the local equilibrium of adherends can be reduced to the following set of differential equations for $j=1,2$:

$$\begin{cases} \frac{dN_j}{dx}=0 \\ \frac{dV_j}{dx}=(-1)^{j+1}bS \\ \frac{dM_j}{dx}+V_j=0 \end{cases} \tag{17}$$

As a result, it comes:

$$S=(-1)^j\left[-\frac{B_j}{b}\frac{d^3u_j}{dx^3}+\frac{D_j}{b}\frac{d^4w_j}{dx^4}\right] \tag{18}$$

Using the constitutive relationship, the adhesive peel stress can be expressed as:

$$S=(-1)^j\frac{D_j}{b}\frac{d^4w_j}{dx^4} \tag{19}$$

In the case of pure mode II loading, the adhesive peel stress vanishes so that the local equilibrium of adherends can be reduced to the following set of differential equations for $j=1,2$:

$$\begin{cases} \frac{dN_j}{dx}=(-1)^jbT \\ \frac{dV_j}{dx}=0 \\ \frac{dM_j}{dx}+V_j+bh_jT=0 \end{cases} \tag{20}$$

As a result, it comes:

$$T=(-1)^j\left[\frac{A_j}{b}\frac{d^2u_j}{dx^2}-\frac{B_j}{b}\frac{d^3w_j}{dx^3}\right] \tag{21}$$

Using the constitutive relationships, the adhesive shear stress can be expressed as:

$$T=(-1)^j\frac{A_j}{b}\frac{d^2u_j}{dx^2} \tag{22}$$

In the case of mixed-mode I/II loading, the local equilibrium of adherends is given by Eq. (5). The following expressions for the adhesive peel and shear stresses are obtained:

$$S=\left[(-1)^j\frac{D_j}{b}-h_j\frac{B_j}{b}\right]\frac{d^4w_j}{dx^4}+\left[h_j\frac{A_j}{b}-(-1)^j\frac{B_j}{b}\right]\frac{d^3u_j}{dx^3} \tag{23}$$

$$T=(-1)^j\left[\frac{A_j}{b}\frac{d^2u_j}{dx^2}-\frac{B_j}{b}\frac{d^3w_j}{dx^3}\right] \tag{24}$$

The same hypotheses as for the ME model are used for the direct method, so that its application on numerical test results with a suitable post processing method provides predictions exactly corresponding to those of ME. A design of experiments is then developed to investigate the main factors influencing the predictions of the direct method.

3. Assessing our methodology of derivatives of deflection with DIC experimental parameters

3.1. Signal processing of the 3rd order derivative of the deflection

Within the framework of the direct method, the evolution of the adhesive stresses can be theoretically derived from the measurement at the crack tip of the second and third order derivative of the upper adherend bending angle and of the derivative of

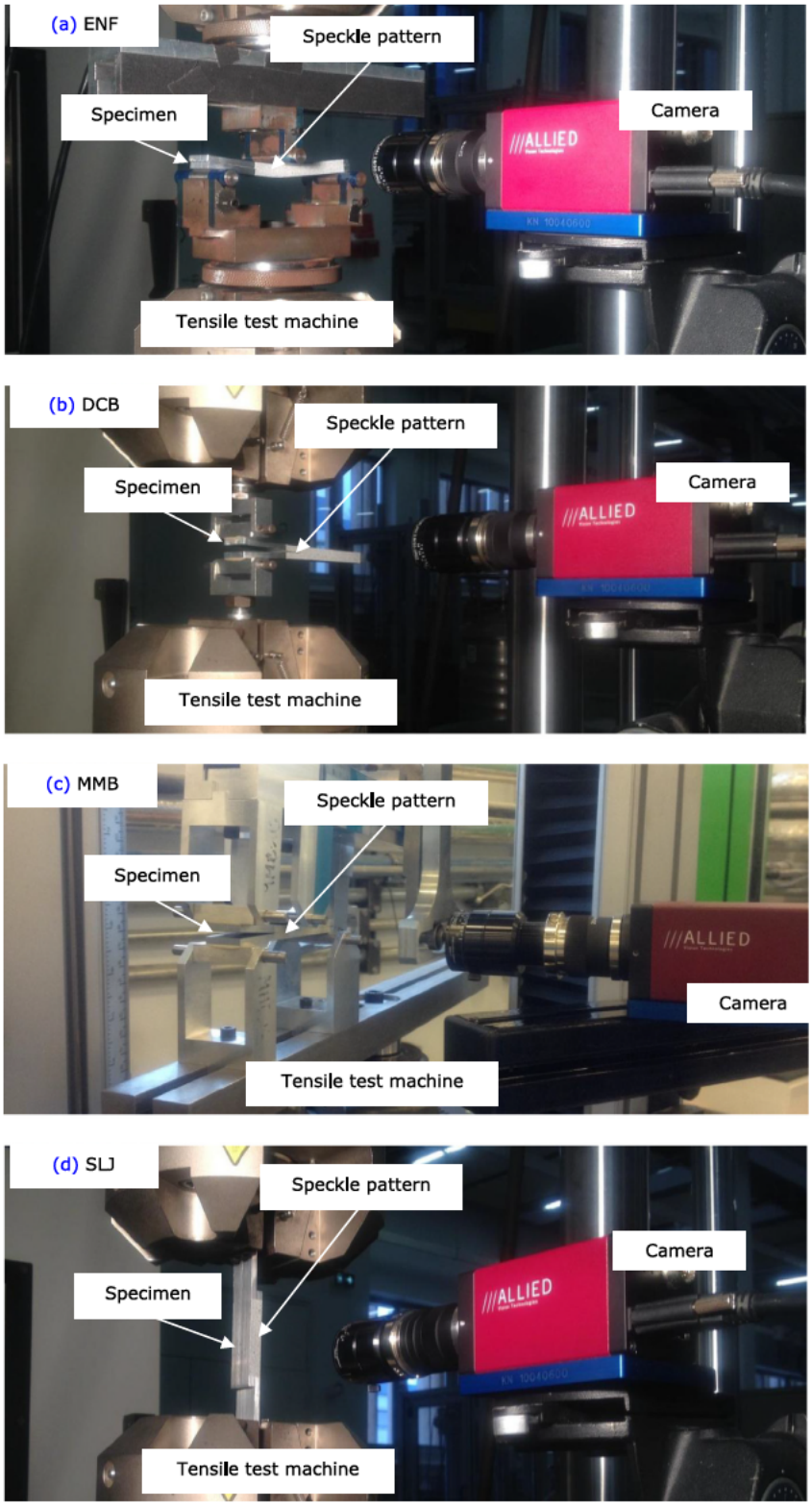

Fig. 22. Experimental monitoring of the adherend-to-adherend displacement field using digital image correlation (DIC) techniques. (a) End notched flexure (ENF) joint specimen. (b) Double cantilever beam (DCB) joint specimen. (c) Mixed-mode bending (MMB) joint specimen. (d) Single-lap joint (SLJ) joint specimen.

the upper adherend longitudinal displacement at neutral axis (see Section 2.5).

Since the raw differentiation of noised experimental results can lead to the rise of important numerical singularities, a particular attention has to be given to the correct evaluation of these successive derivatives. Data pre-processing is then highly needed to reduce experimental noises (see Fig. 14). The data pre-processing algorithm used to reduce experimental noises from the measured upper and lower adherends displacement fields lies on the optimal sub-rank approximation (OSRA) based on singular value

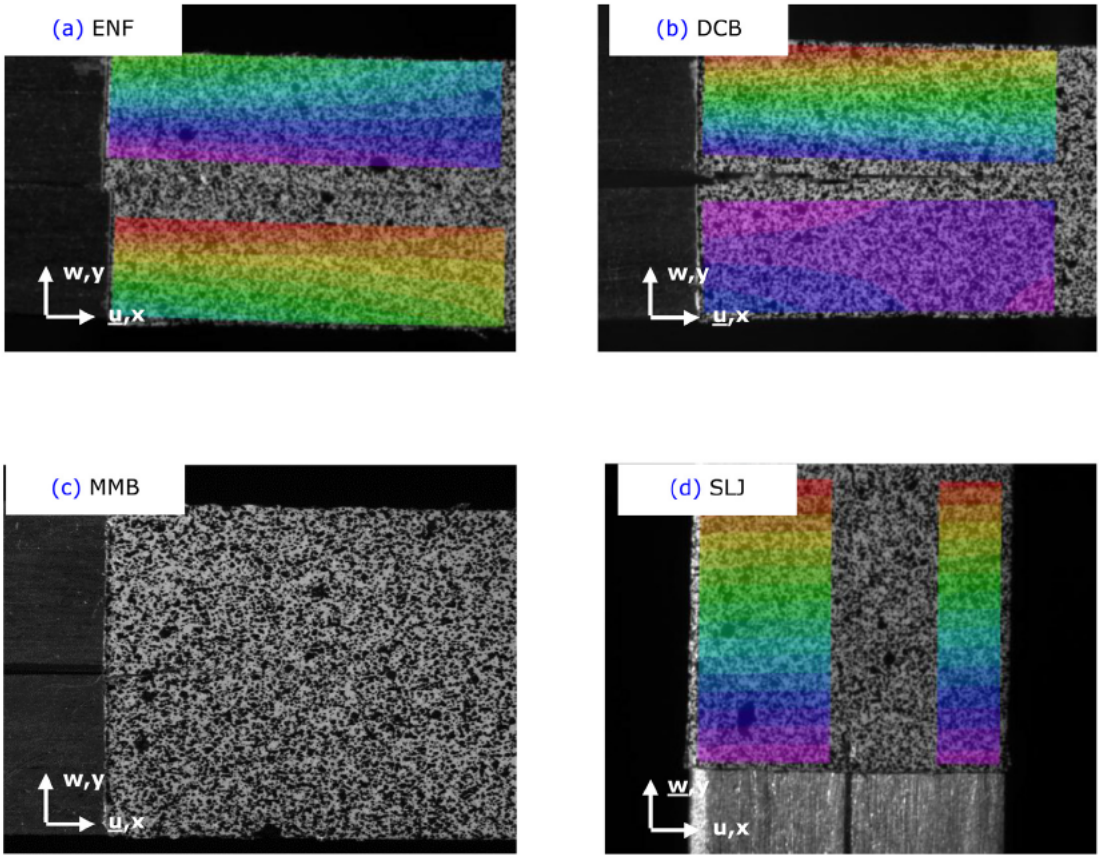

Fig. 23. Experimental monitoring of the adherend-to-adherend displacement field using digital image correlation (DIC) techniques. (a) End notched flexure (ENF) joint specimen. (b) Double cantilever beam (DCB) joint specimen. (c) Mixed-mode bending (MMB) joint specimen. (d) Single-lap joint (SLJ) joint specimen.

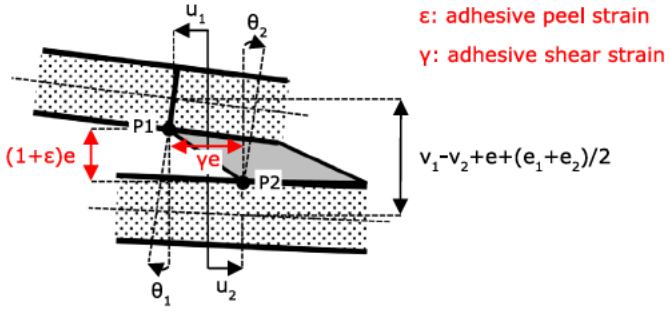

Fig. 24. Schematic representation for the geometrical relationships between both shear and peel deformations of the adhesive layer and the relative displacement of the surrounding adherends. γ: adhesive shear strain. ε: Adhesive peel strain. γe: adhesive shear displacement jump between P2 and P1. $(1+\varepsilon)e$: adhesive peel displacement jump between P2 and P1.

decomposition (SVD), and is related to signal processing techniques that are commonly referred to as SVD signal enhancement methods, reduced-rank signal processing or more simply subspace methods (Andrews and Patterson, 1976). The detailed presentation of the data pre-processing is not given in detail in this paper; a summarized description can be found in the Appendix B.

3.2. Supervised experiments using virtual fields

To characterize the ability of the suggested data pre-processing and differentiation algorithm to determine the successive derivatives of the adherend-to-adherend displacement field with sufficient accuracy, we propose to use supervised virtual fields. It refers to the data pre-processing and data differentiation of a displacement field that is virtually generated so that the evolution of its successive derivatives is known in advance of the experiment. For simplification purpose, the comparison between the supervised data and those obtained from the data processing will be made in terms of the 3rd and 4th order derivatives of the transverse displacement of the adherend neutral axis only. However the results are similar with other derivatives

The virtual displacement field is generated using Matlab® R2012b and resumes the kinematic of a classical Euler–Bernoulli's beam in coupled in-plane tension/flexion, so that:

$$\begin{cases} u(x,y,t) = u(x,y=0,t) - y\frac{\partial v(x,y=0,t)}{\partial x} \\ v(x,y,t) = v(x,y=0,t) \end{cases} \tag{25}$$

where the evolutions of $u(x,y=0,t)$ *and* $v(x,y=0,t)$ are arbitrary fixed as:

$$\begin{cases} u(x,y=0,t) = e^{-0.005tx} \\ v(x,y=0,t) = e^{-0.15tx} \end{cases} \tag{26}$$

To model the effect of experimental noises, the virtual displacement field described in Eqs. (25) and (26) is then degraded by adding a normal (Gaussian) noise using the *normrand(0,σ)* Matlab® function, where 0 refers to the prescribed zero mean value and σ to the configurable standard deviation of the normal (Gaussian) noise distribution.

In order to test for the linear dependency between the successive derivatives of the supervised data and those obtained from the fitted polynomial series, the Pearson product-moment correlation

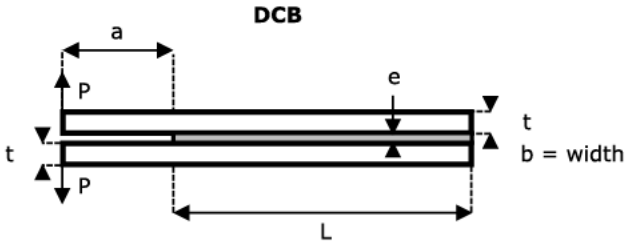

	a	L	t	e	b
Dimensions	30.69mm	70.0mm	3.96mm	0.180mm	22.0mm

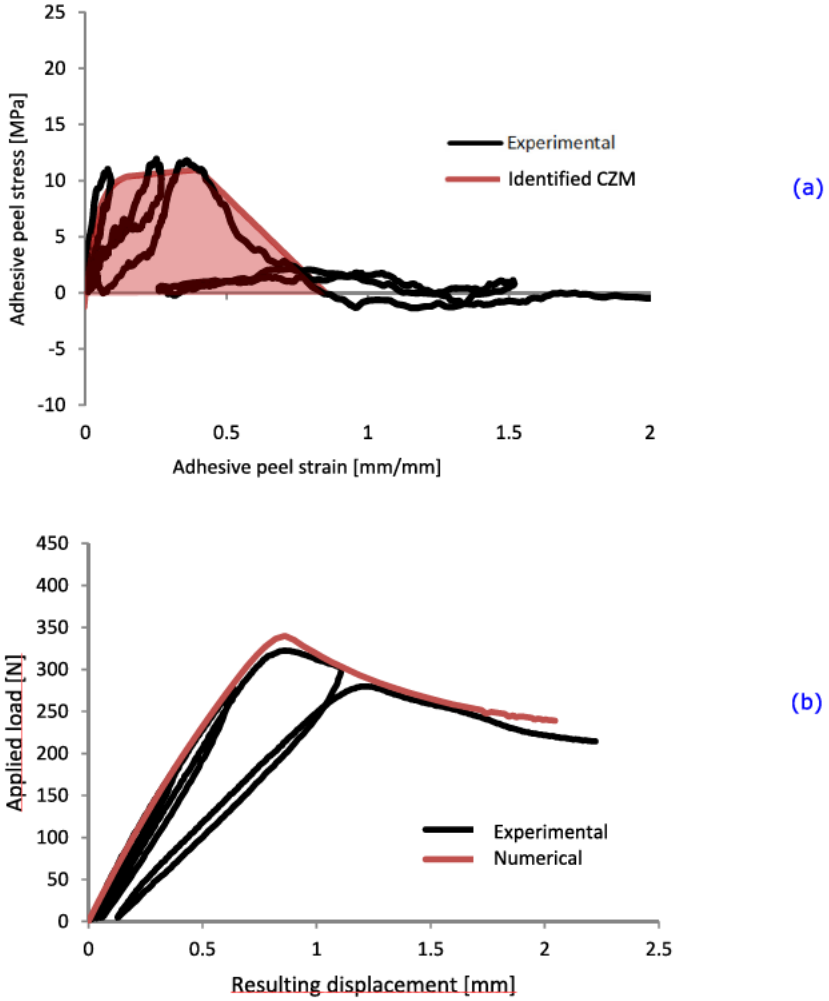

Fig. 25. (a) Experimental adhesive traction separation law in pure mode I. (b) Comparison between experimental results and numerical predictions in terms of load versus displacement curves.

coefficient is used:

$$r = \frac{n(\sum xy) - (\sum x)(\sum y)}{\sqrt{\left[n\sum x^2 - (\sum x)^2\right]\left[n\sum y^2 - (\sum y)^2\right]}} \tag{27}$$

where x refers to the set of supervised data, y to the set of simulated data and n to the total number of data pairs.

3.3. Chosen DOE and justification

A full factorial design of experiments (DoE) consists in the following: (i) vary one factor at a time, (ii) perform experiments for all levels and combination of levels for all factors, (iii) hence perform a large number of experiments (N), (iv) so that all effects and interactions are captured. Let k be the number of factor, n_i the number of levels of the ith factor and p the number of replications to determine the impact of the measurement dispersion. The total

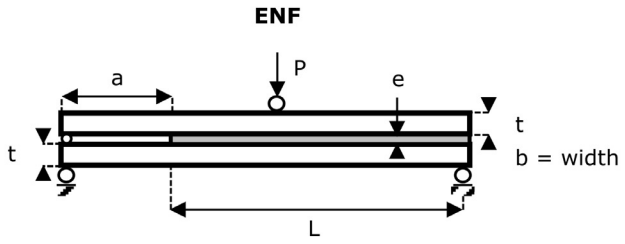

	a	L	t	e	b
Dimensions	29.82mm	71.34mm	3.96mm	0.230mm	22.0mm

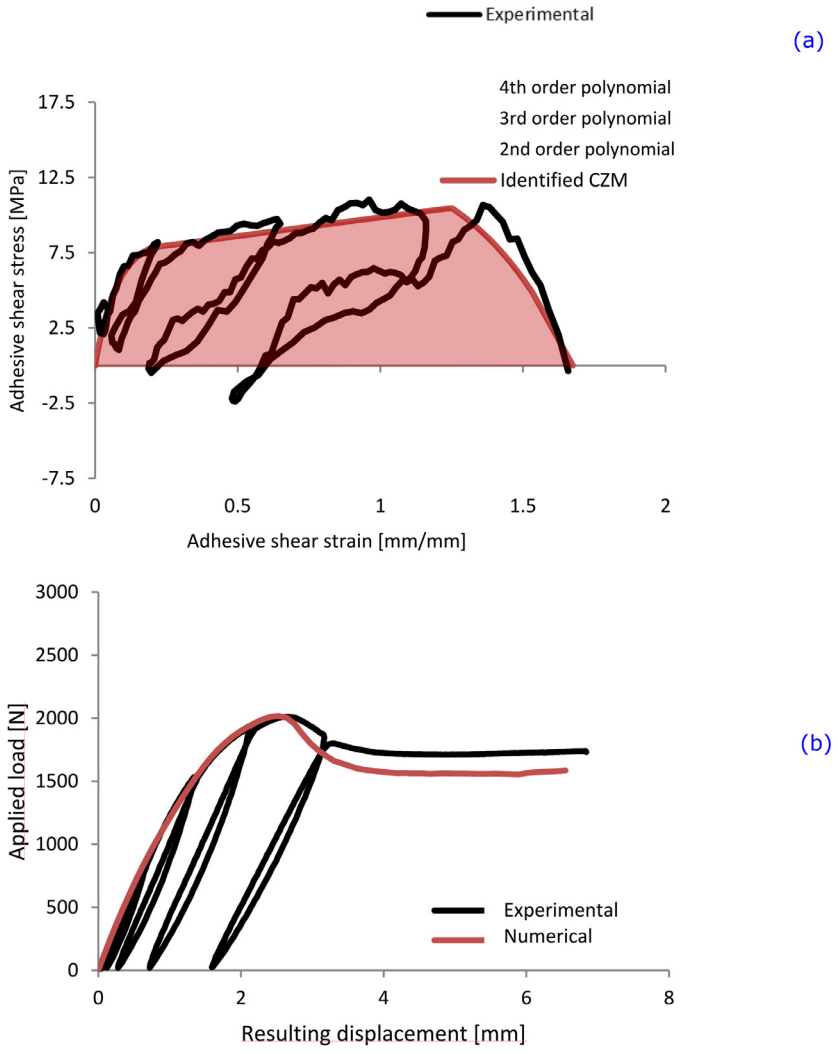

Fig. 26. (a) Experimental adhesive traction separation law in pure mode II. (b) Comparison between experimental results and numerical predictions in terms of load versus displacement curves.

number of experiments N of a full factorial DoE is then:

$$N = p\left(\prod_{i=1}^{k} n_i\right) \tag{28}$$

Here is considered a full factorial DoE of five factors with respectively $3 \times 3 \times 3 \times 3 \times 2$ levels, so that the linear Taguchi's graph of effects and interactions can be represented in the form of Fig. 15.

In Fig. 15, the main effects and interactions are represented, termed respectively $E(\mathrm{i})$ and $I(\mathrm{ij})$, of factors $i,j = A, B, C, D$ and E onto the objective function that is r^2. Each experiment is replicated 15 times to capture the impact of the measurement dispersion, so that the total number of experiments is $(3 \times 3 \times 3 \times 3 \times 2) \times 15 = 2430$. The different factor levels are given in Table 3. where SNR refers to the simulated Signal-to-Noise ratio, $x = y$ to the spatial resolution of each displacement field instantaneous image, t to the number of instantaneous images taken during the experiment

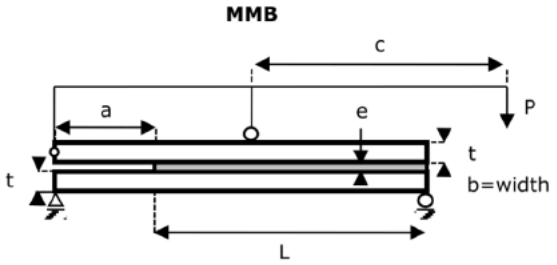

	a	L	t	e	b
Dimensions	30.21mm	70.89mm	3.96mm	0.180mm	22.0mm

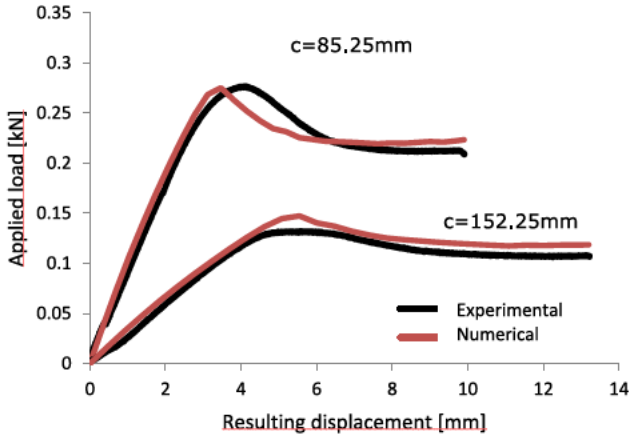

Fig. 27. Determination of the effective mixed-mode properties of the adhesive layer using the inverse method. Comparison between experimental results and semi-analytical predictions in terms of load versus displacement curve.

Table 3
Factor versus levels matrix.

	SNR^{-1} (A)	$x=y$ (B)	t (C)	Degree (D)	Model (E)
Low (−1)	0.00175	201	51	4	1
Medium (0)	0.00350	401	101	6	N.A
High (+1)	0.00700	801	201	8	2

(i.e. thereafter referred as the temporal resolution), *Degree* to the degree of the polynomial series used to fit/differentiate the neutral fiber transverse displacement and *Model* to the model used for minimizing the vertical deviation with experimental data in the sense of the least squares method (1 means fitting independently on $v(x)$ and on $\theta(x)=dv(x)/dx$, 2 means fitting simultaneously $v(x)$ and $\theta(x)=dv(x)/dx$).

3.4. Synthesis of the results

The initial SNR appears as a key parameter in increasing the accuracy of measuring the successive derivatives of the upper adherend displacement field (see Fig. 16(a)), then suggesting that a significant attention has to be given into reducing the noise of the measured signal before any pre-processing of the data. This can be achieved in various ways so that it results in improving the overall quality of the displacement measures.

The spatial resolution of the instantaneous images of the upper adherend displacement field also appears as a key parameter in increasing the accuracy of the estimation of the successive derivatives of the upper adherend displacements (see Figs. 16(b) and 17(e),(h)). A particular attention has then to be given to measuring the displacements of the upper adherend with a sufficient enough spatial resolution.

On another side, the time resolution (i.e. number of images of the upper adherend displacement field taken during the experiment) appears as negligibly influencing the accuracy of the estimation of the successive derivatives of the upper adherend displacements (see Figs. 16(c) and 17(b), (d), (f) and (i)). Thus its own effect as well as its respective interactions with other factors can be legitimately neglected at first sight.

Similarly to the initial SNR or the spatial resolution of the displacement images, the degree of the polynomial series used for fitting/differentiating the pre-processed displacements also appears as a parameter that has to be chosen with extreme caution. Indeed, although increasing the degree of the polynomial series from 4 to 6 appears as negligibly influencing the overall accuracy of the measure, increasing it from 6 to 8 results in a serious degradation of the accuracy of the measure (see Fig. 16(d)). This degradation of the accuracy of the measurement using high order polynomials is a well-known issue, and is due to the oscillation of the polynomial series around the experimental set of data points for increasing degrees (i.e. Runge's phenomenon). A particular attention has then to be given in choosing the best compromise between fitting the experimental data points using high order polynomials functions and preserving the overall accuracy of the measurement of its successive derivatives.

Finally, the choice of the Moore–Penrose pseudo inverse model for minimizing in the sense of the least squares method the vertical deviation between the polynomial function (i.e. used for fitting/differentiating the set of experimental data points) and the experimental data points themselves appears as a worthwhile way of

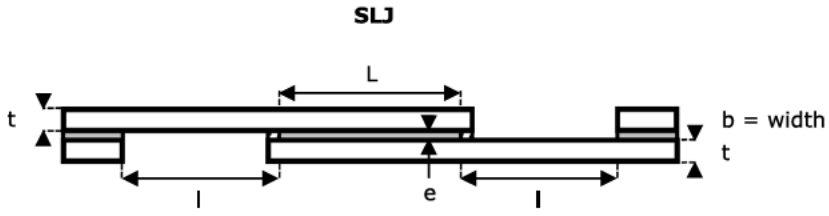

	L	l	t	e	b
Dimensions	51.4mm	29.35mm	3.96mm	0.120mm	22.0mm

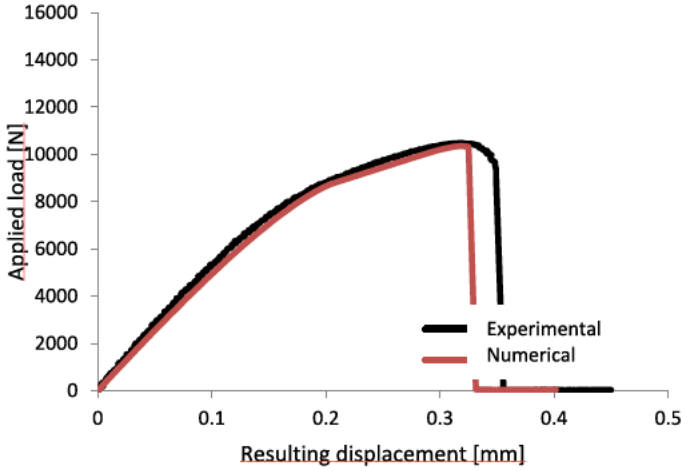

Fig. 28. Comparison between experimental results and semi analytical predictions in terms of load versus displacement curve.

influencing the accuracy of the measured displacement derivatives (see Fig. 16(e)). It is then suggested that simultaneously accounting for both $v(x)$ and $\theta(x) = dv(x)/dx$ when fitting/differentiating the experimental set of data points significantly increases the accuracy of the measurement.

4. Experimental test campaign

The entire test campaign is performed on an electro-mechanical test machine (Ref: Instron AI735-1325).

4.1. Adherend bulk specimens

Each specimen is manufactured from a laminated aluminum-magnesium-silicon alloy (6060 series). A total of three specimens are tested. The manufactured specimens are measured before the tests (see Fig. 18). The evolution of both the applied load and the resulting displacement are measured using the build-in machine load and displacement cells. The loading speed is fixed at 0.5 mm/min. The evolution of the specimen displacement field is measured using the digital image correlation (DIC) technique (see Fig. 19). Both the evolution of the axial deformation and the Poisson's ratio of the samples are computed from the evolution of the specimen displacement field. The specimens are displacement loaded using the build-in machine displacement command instruction. The results obtained in terms of (a) the axial stress-strain evolution law and (b) the evolution of the measured Poisson's ratio as a function of the axial deformation in Fig. 20. The aluminum alloy exhibits two distinct phases. The first one, the linear elastic phase, appears as extremely limited compared to the whole deforming capability of the material (i.e. ~3% of the whole deforming capability of the material). The second phase, the plasticization phase (Bartczak and al., 2010), appears on another side as extremely important (i.e. ~97% of the whole deforming capability of the material). To model the effective stress-strain evolution law of each adherend, it is then decided to fit a trilinear elastic-plastic evolution law onto the results obtained (see Fig. 21). The material law identified is provided in Table 4. A Poisson's ratio of 0.35 is considered.

4.2. Adhesive joint specimens

4.2.1. Overview of the experimental setting

The adhesive used is the SAF30 MIB adhesive from AEC Polymers / BOSTIK (ARKEMA Group). It is a methacrylate-based two-component adhesive paste. In order to enhance the adhesion properties between the adhesive layer and each adherend before bonding, both adherends are cleaned using the AEC Polymers T700 dry cleaning spray. In order to ensure a constant adhesive thickness along the overlap, two calibrated anti-adhesive tapes are stuck at each side of the bonded overlap (see Fig. 3). The dimensions of each specimen are controlled after bonding (see Table 5). The applied load, the resulting displacement and the adherend-to-adherend displacement field at crack tip are measured during the tests. The evolution of both the applied load and the resulting displacement are measured using the build in machine load and displacement cells. The load speed is 0.5 mm min^{-1}. The evolution of the adherend-to-adherend displacement field is measured using the DIC technique (see Figs. 22 and 23). The pure mode deformations of the adhesive layer are computed from the relative displacement of the adherends neutral fibers (see Fig. 24). Both DIC and build-in machine measures are synchronized using an analogical-to-numerical National Instrument acquisition card, so that it facilitates the processing of the adhesive CZM constitutive

Table 4
Definition of aluminum bulk material law identified. σ = true stress. ε = true strain.

	Elastic	Plastic 1	Plastic 2
Model (EPB)	$\sigma(\varepsilon)=E\varepsilon$	$\sigma(\varepsilon)=\sigma_1+E_{T,1}(\varepsilon-\varepsilon_1)$	$\sigma(\varepsilon)=\sigma_2+E_{T,2}(\varepsilon-\varepsilon_2)$
		$E_{T,1}=8800\text{MPa}$	$E_{T,2}=250\text{MPa}$
Parameters	$E=66000\text{MPa}$	$\sigma_1=200.31\text{MPa}$	$\sigma_2=232.84\text{MPa}$
		$\varepsilon_1=0.003035$	$\varepsilon_2=0.04$
Validity	$0\le\varepsilon\le\varepsilon_1$	$\varepsilon_1\le\varepsilon\le\varepsilon_2$	$\varepsilon_2\le\varepsilon$

Table 5
Controlled geometries of the ENF, DCB, MMB and SLJ joint specimens.

	a	L	l	t	e	b
ENF	29.82 mm	71.43 mm	N.A.	3.96 mm	0.230 mm	22.0 mm
DCB	30.69 mm	70.0 mm	N.A.	3.96 mm	0.180 mm	22.0 mm
MMB	30.21 mm	70.89 mm	N.A.	3.96 mm	0.180 mm	22.0 mm
SLJ	N.A.	51.4 mm	29.35 mm	3.96 mm	0.120 mm	22.0 mm

Table 6
CZM properties in pure mode I.

	Elastic	Plastic	Softening
Model (CZM)	$S(\varepsilon)=\frac{k_S\varepsilon_1}{\ln(e_S)}(1-\exp(\frac{\ln(e_S)}{\varepsilon_1}\varepsilon))$	$S(\varepsilon)=S_1+k_{S,1}(\varepsilon-\varepsilon_1)$	$S(\varepsilon)=S_2\frac{\varepsilon_3-\varepsilon}{\varepsilon_3-\varepsilon_2}$
	$k_S=250\text{MPa}$	$k_{S,1}=2.5\text{MPa}$	$S_2=10.99\text{MPa}$
Parameters	$e_S=0.030$	$S_1=10.37\text{MPa}$	$\varepsilon_2=0.4$
	$\varepsilon_1=0.15$	$\varepsilon_1=0.15$	$\varepsilon_3=0.75$
Validity	$0\le\varepsilon\le\varepsilon_1$	$\varepsilon_1\le\varepsilon\le\varepsilon_2$	$\varepsilon_2\le\varepsilon\le\varepsilon_3$

Table 7
CZM properties in pure mode II.

	Elastic	Plastic	Softening
Model (CZM)	$T(\gamma)=\frac{k_T\gamma_1}{\ln(e_T)}(1-\exp(\frac{\ln(e_T)}{\gamma_1}\gamma))$	$T(\gamma)=T_1+k_{T,1}(\gamma-\gamma_1)$	$T(\gamma)=T_2\frac{\gamma_3{}^3-\gamma^3}{\gamma_3{}^3-\gamma_2{}^3}$
	$k_T=110\text{MPa}$	$k_{T,1}=2.5\text{MPa}$	$T_2=10.48\text{MPa}$
Parameters	$e_T=0.075$	$T_1=7.85\text{MPa}$	$\gamma_2=1.25$
	$\gamma_1=0.2$	$\gamma_1=0.2$	$\gamma_3=1.675$
Validity	$0\le\gamma\le\gamma_1$	$\gamma_1\le\gamma\le\gamma_2$	$\gamma_2\le\gamma\le\gamma_3$

relationships. The mechanical stiffness of the tensile test machine is characterized so that the resulting displacement measured by the build-in machine displacement cell is corrected to fit the true displacement of the adhesive test specimens. Four specimens of each configuration (e.g. ENF, DCB, MMB and SLJ) are tested. The SLJ specimens are tested for relevance assessment purposes only. Correlations between experimental and numerical force versus resulting displacement curves are used to assess the ability of the direct approach to characterize the CZM properties. A particular emphasis is given to the ability of the suggested approach to provide both the experimental stiffness and the maximum load bearing capability of each adhesive specimen. All the numerical tests presented in this paper are based on the simplified stress analyses using ME, already presented in details in (Lélias et al., 2015).

4.2.2. Test results and modelling under pure modes

The constitutive traction separation law of the adhesive layer obtained in the case of pure mode I and pure mode II loadings is presented in Figs. 25-(a) and 26-(a) respectively. The CZM parameters for pure mode I and pure mode II l are then provided in Tables 6 and 7 respectively. On each pure mode, the model obtained is composed by 3 parts: an elastic part, a plastic part and a softening part. The identification of CZM parameters is performed on the envelope curves built from the cyclic response, using the elastic stiffness of adherends. The hypothesis underlying is that the Young's modulus does not vary significantly during the plastic phase. Even if this hypothesis does not hold at large strain of adherends, it allows drastic simplification of the identification process. It means that the adherend stiffnesses used for the identification in Eqs. (18), (21), (23) and (24) correspond to the initial elastic values. A numerical test is then performed assuming a nonlinear behavior for both the adherends (following the trilinear approximation in Table 4, see Appendix C) and the adhesive layer. The numerical test predictions, in terms of load / displacement curve, are then compared to the experimental test results on DCB and ENF specimens in Figs. 25-(b) and 26-(b) respectively. A good agreement is shown.

4.2.3. Test results and modelling under mixed-mode I/II

As previously, the constitutive relationships of the adhesive layer when facing mixed-mode I/II solicitations are investigated using the direct method. Nevertheless, the exploitation of test results fails, due to the limited axial displacements of both upper and lower adherends nearby the adhesive crack tip. It results in badly conditioned measures of the adherends axial displacements, from which the differentiation with respect to x is insufficiently accurate. An alternative characterization method is then developed for determining the effective mixed-mode I/II properties of the tested MMB specimens. It is suggested to use an inverse characterization method based on numerical tests. The CZM properties in pure mode I and pure mode II are considered as well as the nonlinear adhered behavior. Both initiation and propagation mixed-mode criteria are assumed as following power law energetical relationships (see Eq. (7)). The idea is then to adjust the value of the value of the exponent $n=m$ in order numerical prediction fit the experimental tests. In this study, the identification was made according to tests with two different value of mixed-mode ratio, by the use of two different lever arm denoted c. Similarly to the previous pure mode tests, the experimental test results and numerical test predictions for both mixed-mode ratios are compared in terms of

load / displacement curve in Fig. 27. The presented comparison is for $n=m=1$. Good agreement is shown.

In order to assess the relevance of the measured constitutive stress-strain relationships of the adhesive layer subjected to pure mode I, pure mode II and mixed-mode I/II adhesive loadings, experimental test results and numerical test predictions are compared on the configuration of the SLJ configuration. As shown, in Fig. 28, good agreement is shown in terms of both stiffness and maximum load bearing capability of the SLJ joint specimen. Nevertheless, the single-lap joint configuration is known to be submitted significantly more in mode I than in mode II due to the eccentricity of the load path generating secondary bending moment and large peel stresses at both overlap ends. To validate the behavior law under mixed-mode, other experimental tests should be conducted based on various loading and geometrical configurations.

5. Conclusion

In this paper, a direct method for the assessment of the CZM parameters of a thin adhesive layer is presented and then implemented. This method is based on the measurement of the displacement field of adherends at the crack tip of classical adhesively bonded specimens (i.e.: ENF, DCB, MMB), allowing for pure mode I, pure mode II and mixed-mode I/II loadings. Nevertheless, the identification presented remains dependent of the modelling framework. The experimental implementation makes use of a methacrylate-based two-component adhesive paste, found under the commercial reference SAF30 MIB manufactured by AEC Polymers / Bostik (ARKEMA Group). The adherends are made in aluminum alloy (6060 series). The adhesive constitutive stress-strain relationships are derived from the monitoring of the evolution at crack tip of both the relative displacement of interfaces and the displacement field of the adherend, using the DIC technique. The main difficulty encountered within the experimental implementation concerns the experimental measurements. Indeed, a dedicated data preprocessing (see Appendix B) is developed to best fit the experimental data coming from the DIC technique. The use of experimental measurement providing a higher resolution such as Speckle interferometry could be more suitable.

In pure mode I and pure mode II, it is shown that the adhesive layer experiences three distinct phases. The first one, the linear elastic phase, appears as extremely limited compared to the whole deforming capability of the adhesive layer. A mathematical model is then provided for each mode. Under mixed-mode, the data preprocessing fails in interpreting the experimental measurements, so that a dedicated method is suggested. The mathematical models are then implemented to perform numerical tests using a simplified stress analysis based on ME. In terms of global behavior, the predictions of numerical tests are in a close agreement with the results of experimental tests, up to the final failure of specimens. Besides, it is indicated that the identification of CZM properties presented in this paper involves specimens, the adherends of which experienced plasticization. Even if the simplified stress analysis based on ME allowing for numerical tests supports both nonlinear adhesive and adherend material behavior, the embedded level of complexity in the experimental test procedure appears as elevated. The implementation of the direct method should be then tested through various combinations of adherends and adhesive materials and various geometries, some of which should prevent the adherends to plasticize, to assess the reliability of the experimental procedure. The effect of the adhesive thickness on the material law could be investigated using measurement means with a better performance.

Acknowledgment

The authors gratefully acknowledge Mr Christian Bret, CEO of AEC Polymers, for the supplying of materials.

Appendix A

Considering the local equilibrium equations Eq. (8), the adhesive stresses are replaced by their expressions as functions of adherend displacements Eq. (9). In conjunction Eq. (10), it results in a system of twelve linear first-order ordinary differential:

$$\begin{cases} \frac{du_1}{dx} = \frac{D_1}{\Delta_1}N_1 + \frac{B_1}{\Delta_1}M_1 \\ \frac{du_2}{dx} = \frac{D_2}{\Delta_2}N_1 + \frac{B_2}{\Delta_2}M_2 \\ \frac{dv_1}{dx} = \theta_1 \\ \frac{dv_2}{dx} = \theta_2 \\ \frac{d\theta_1}{dx} = \frac{B_1}{\Delta_1}N_1 + \frac{A_1}{\Delta_1}M_1 \\ \frac{d\theta_2}{dx} = \frac{B_2}{\Delta_2}N_2 + \frac{A_2}{\Delta_2}M_2 \\ \frac{dN_1}{dx} = bk_{II}u_1 + bk_{II}h_1\theta_1 - bk_{II}u_2 + bk_{II}h_2\theta_2 \\ \frac{dN_2}{dx} = -bk_{II}u_1 - bk_{II}h_1\theta_1 + bk_{II}u_2 - bk_{II}h_2\theta_2 \\ \frac{dV_1}{dx} = bk_I v_1 - bk_I v_2 \\ \frac{dV_2}{dx} = -bk_I v_1 + bk_I v_2 \\ \frac{dM_1}{dx} = bh_1k_{II}u_1 + bk_{II}h_1h_1\theta_1 - bh_1k_{II}u_2 + bk_{II}h_1h_2\theta_2 - V_1 \\ \frac{dM_2}{dx} = bh_2k_{II}u_1 + bk_{II}h_2h_2\theta_1 - bh_2k_{II}u_2 + bk_{II}h_2h_2\theta_2 - V_2 \end{cases} \tag{A1}$$

This system can be written as $\frac{dX}{dx} = AX$ where A is 12×12 matrix with real constant components and the unknown vector X such that ${}^tX = (u_1\ u_2\ v_1\ v_2\ \theta_1\ \theta_2\ N_1\ N_2\ V_1\ V_2\ M_1\ M_2)$. But the elementary stiffness matrix corresponds to the relationship between the vector of nodal forces and the vector of nodal displacements (Paroissien, 2006a; Paroissien et al., 2006b, 2007, 2013; Lélias et al., 2015), such as:

$$\begin{pmatrix} -N_1(0) \\ -N_2(0) \\ N_1(\Delta) \\ N_2(\Delta) \\ -V_1(0) \\ -V_2(0) \\ V_1(\Delta) \\ V_2(\Delta) \\ -M_1(0) \\ -M_2(0) \\ M_1(\Delta) \\ M_2(\Delta) \end{pmatrix} = K_{BBe} \begin{pmatrix} u_1(0) \\ u_2(0) \\ u_1(\Delta) \\ u_2(\Delta) \\ v_1(0) \\ v_2(0) \\ v_1(\Delta) \\ v_2(\Delta) \\ \theta_1(0) \\ \theta_2(0) \\ \theta_1(\Delta) \\ \theta_2(\Delta) \end{pmatrix} \tag{A2}$$

The fundamental matrix of A, termed Φ_A, is computed at $x=0$ and $x=\Delta$; using the SCILAB software, the associated command is "expm":

$$\begin{cases} \Phi_A(x=0) = expm(A.0) \\ \Phi_A(x=\Delta) = expm(A.\Delta) \end{cases} \tag{A3}$$

From these both 12*12 matrices, two matrices M' and N' are extracted. M' (N') is composed of the lines related to the nodal displacements (forces). For each, a first block of six lines and twelve

rows comes from $\Phi_A(x=0)$ and the second block of six lines and twelve rows come from $\Phi_A(x=\Delta)$, such that:

$$\begin{cases} M' = \Phi_U(0,\Delta) = \begin{pmatrix} [\Phi_A(x=0)]_{i=1,2,3,4,5,6;\, j=1:12} \\ [\Phi_A(x=\Delta)]_{i=1,2,3,4,5,6;\, j=1:12} \end{pmatrix} \\ N' = \Phi_F(0,\Delta) = \begin{pmatrix} [\Phi_A(x=0)]_{i=7,8,9,10,11,12;\, j=1:12} \\ [\Phi_A(x=\Delta)]_{i=7,8,9,10,11,12;\, j=1:12} \end{pmatrix} \end{cases} \quad \text{(A4)}$$

where i (j) indicates the line (row) number.

As K_{BBe} is defined according to $[u_1(0)\ u_2(0)\ u_1(\Delta)\ u_2(\Delta)\ v_1(0)\ v_2(0)\ v_1(\Delta)\ v_2(\Delta)\ \theta_1(0)\ \theta_2(0)\ \theta_1(\Delta)\ \theta_2(\Delta)]$, a simple rearrangement of the order of lines of M' is performed to produce the matrix M. Similarly, the matrix N' is submitted to the same operation. In a same way, the terms related to nodal forces at $x=0$ are multiplied by -1 to follow the arrangement $[-N_1(0)\ -N_2(0)\ N_1(\Delta)\ N_2(\Delta)\ -V_1(0)\ -V_2(0)\ V_1(\Delta)\ V_2(\Delta)\ -M_1(0)\ -M_2(0)\ M_1(\Delta)\ M_2(\Delta)]$. It leads to the definition of the matrix N. The elementary stiffness matrix K_{BBe} is equal to the product of N and the inverse of M (Paroissien et al., 2013; Lélias et al., 2015): $K_{BBe}=N.M^{-1}$.

Even if it is not the topic of this paper, it is obvious that this previous approach can be easily used to develop ME, under different local equilibrium equations (e.g. Hart-Smith (Hart-Smith 1973; Luo and Tong 2009; Paroissien et al., 2018) or under different constitutive equations (e.g. Tsai et al., 1998) and/or including different number layers of adhesives and adherends (e.g. double lap joint configuration). It is indicated that the resolution using the exponential matrix was already been used in previous works (Gustafson et al., 2006; Gustafson and Waas, 2007; Gustafson, 2018; Gustafson and Waas, 2009; Stapleton and Waas, 2007; Stapleton et al., 2010; Stapleton, 2012; Stapleton et al., 2012; Stapleton et al., 2017). The use of the resolution scheme using the exponential matrix is suitable in the case of nonlinear analysis since a mesh is required. It is suitable in the case of non-homogeneous elastic adhesive properties too (Paroissien et al., 2018). Besides, it is useful for the formulation of new macro-elements under various simplified hypotheses (Paroissien et al., 2018).

Appendix B

The data pre-processing algorithm used to reduce experimental noises from the measured adherend-to-adherend displacement fields then lies on the digital mapping of the adherend-to-adherend axial (transverse) displacement fields as a set of 2D matrices. First, the evolution of the axial (transverse) displacement field of each adherend is mapped as 3D tensors resuming both the distributions of the adherend axial (transverse) displacements nearby the adhesive crack tip as well as their respective evolutions. Then, the constructed 3D tensors of dimensions x, y and t are rearranged in the form of simpler 2D matrices so that their new dimensions are respectively y and x^*t (see Fig. B1). The constructed 2D matrices are then filtered using the rank-R reduction approximation based on the SVD of the raw experimental results, so that R is chosen to capture 95% of the original data energy in the sense of the Frobenius norm (see Fig. B2). The evolution of each adherend axial and transverse displacement fields are then reconstructed from their respective decompositions and rearranged in the form of 3D tensors, so that the displacements of the upper (lower) neutral fiber are finally extracted from the reconstructed axial and transverse displacement fields and formatted into the relevant beam or plate theory (see Fig. B3). Finally, the differentiation of the adherends cross-section rotation is ensured by fitting a polynomial series so that the vertical deviation with experimental data is minimized in the sense of the least squares method by using the Moore–Penrose pseudo inverse technique.

Besides, a full factorial design of experiments is performed in order to assess the algorithmic parameters on the accuracy of the measure. It consists in the following: (i) vary one factor at a time, (ii) perform experiments for all levels and combination of levels for all factors, (iii) hence perform a large number of experiments, (iv)

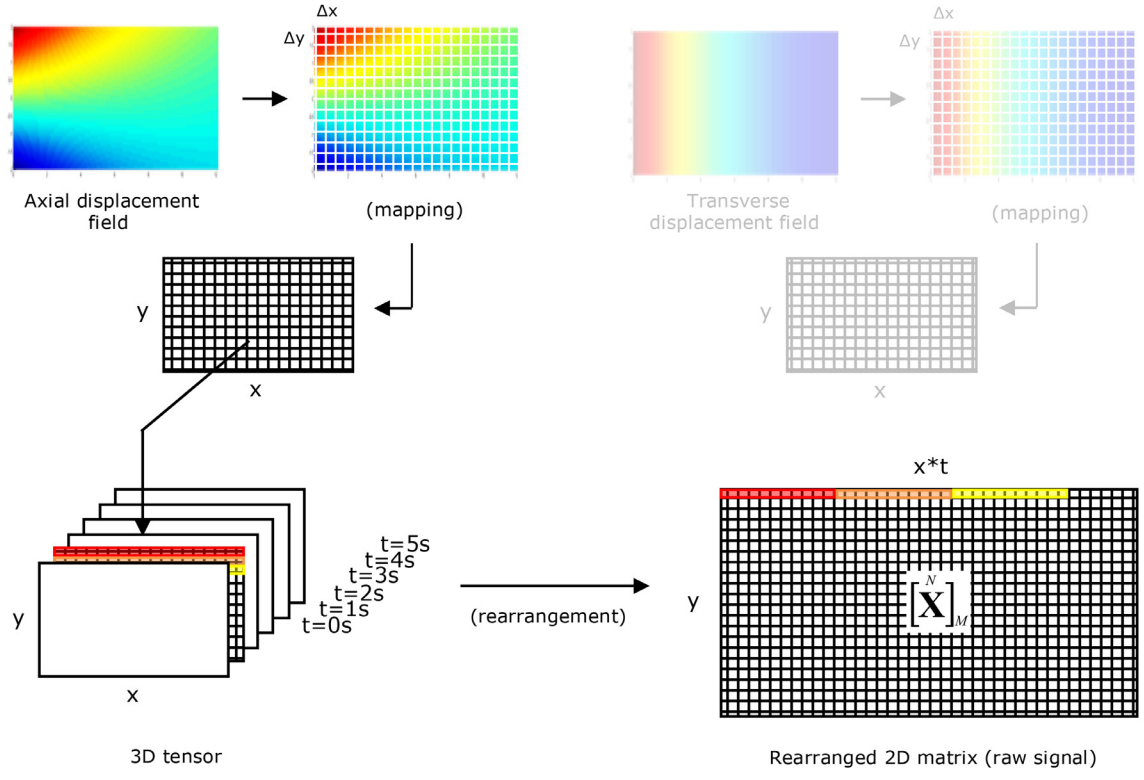

Fig. B.1. Digital mapping of the adherend-to-adherend axial and transverse displacement fields.

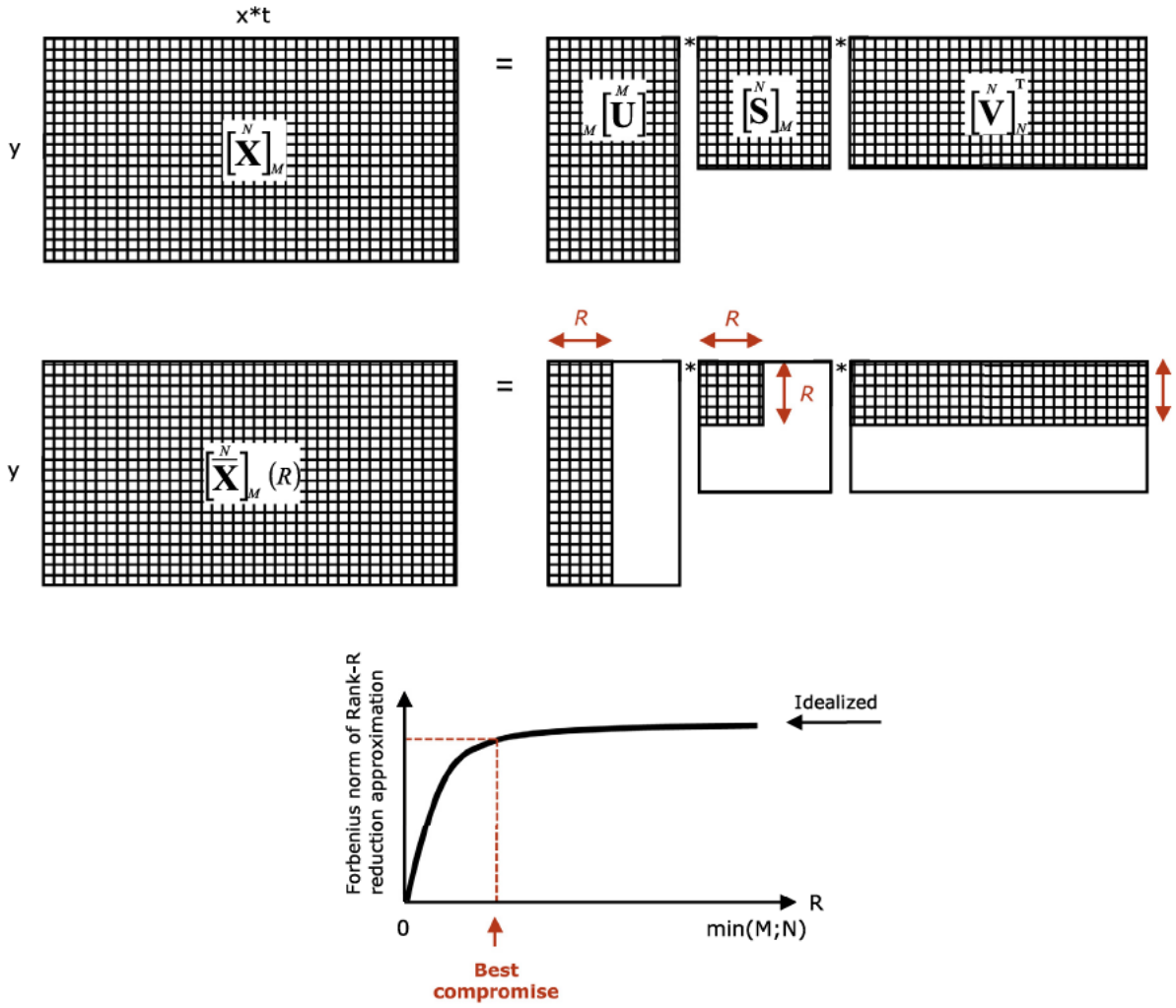

Fig. B.2. Filtering of the experimental results using the rank-R reduction approximation based on Singular Value Decomposition (SVD).

so that all effects and interactions are captured. The main results for each of five factors selected are presented hereafter.

(I) The initial signal to noise ratio appears as a key parameter in increasing the accuracy of measuring the successive derivatives of the upper adherend displacement field. It suggests that a significant attention has to be given into reducing the noise of the measured signal before any pre-processing of the data. This can be achieved in various ways so that it results in improving the overall quality of the displacement measures (DIC).

(II) The spatial resolution of the instantaneous images of the upper adherend displacement field also appears as a key parameter in increasing the accuracy of the estimation of the successive derivatives of the upper adherend displacements. A particular attention has then to be given to measuring the displacements of the upper adherend with a sufficient enough spatial resolution.

(III) On another side, the time resolution (i.e. number of images of the upper adherend displacement field taken during the experiment) appears as negligibly influencing the accuracy of the estimation of the successive derivatives of the upper adherend displacements. Its own effect as well as its respective interactions with other factors can be legitimately neglected at first sight.

(IV) Similarly to the initial signal to noise ratio or the spatial resolution of the displacement images, the degree of the polynomial series used for fitting/differentiating the pre-processed displacements also appears as a parameter that has to be chosen with extreme caution. Indeed, although increasing the degree of the polynomial series from four to six appears as negligibly influencing the overall accuracy of the measure, increasing it from six to eight results in a serious degradation of the accuracy of the measure. This degradation of the accuracy of the measurement using high order polynomials is a well-known issue, and is due to the oscillation of the polynomial series around the experimental set of data points for increasing degrees. A particular attention has then to be given in choosing the best compromise between fitting the experimental points using high order polynomials functions and preserving the overall accuracy of the measurement of its successive derivatives.

(V) Finally, the choice of the Moore–Penrose pseudo inverse model for minimizing in the sense of the least squares method the vertical deviation between the polynomial function (i.e. used for fitting/differentiating the set of experimental data points) and the experimental data points themselves appears as a worthwhile way of influencing the accuracy of the measured displacement derivatives. It is then suggested that simultaneously accounting for both $v(x)$ and $\theta(x)=dv(x)/dx$ when fitting/differentiating the experimental set of data points significantly increases the accuracy of the measurement.

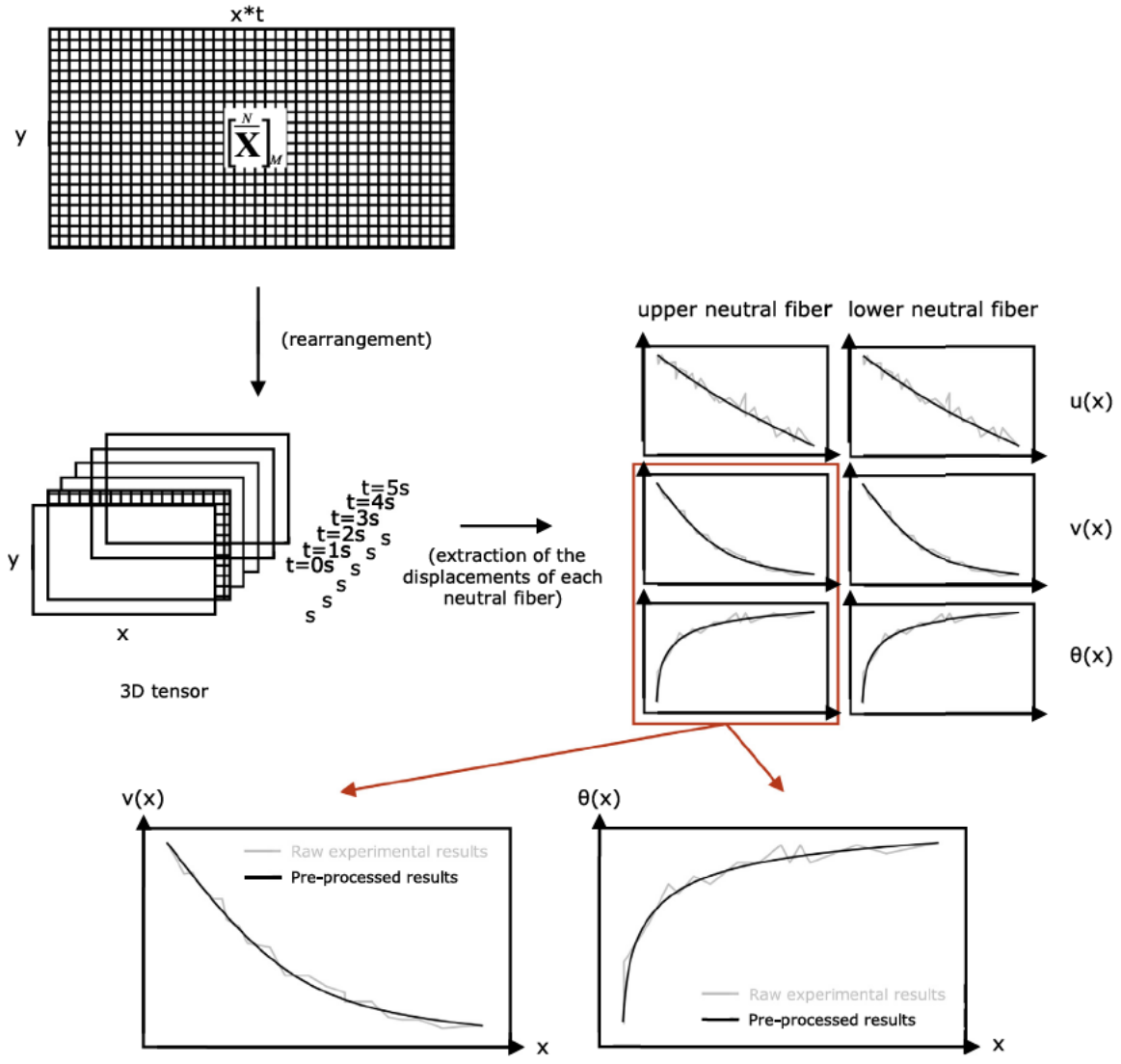

Fig. B.3. Extraction of the displacements of each adherend neutral fiber.

Appendix C

The beam model use for the adherends allows for the consideration of the Young's modulus graduation in the thickness (Clarck, 2003; Weissgraeber and al. 2014). The constitutive equations for the normal force and bending moment are derived as it follows.

Using the Euler–Bernoulli kinematics, the normal force N_j of the adherend j is written such as:

$$N_j = \int \sigma_{xx} dS = \int E_j(y)\varepsilon_{xx} dS = \int E_j(y)\left[\frac{du_j}{dx} - y\frac{d\theta_j}{dx}\right] dS \tag{C-1}$$

It leads to:

$$N_j = \left(\int E_j(y) dS\right)\frac{du_j}{dx} - \left(\int E_j(y) y dS\right)\frac{d\theta_j}{dx} = A_j\frac{du_j}{dx} - B_j\frac{d\theta_j}{dx} \tag{C-2}$$

The same approach is used for the bending moment:

$$M_j = \int -y\sigma_{xx} dS = \int -yE_j(y)\varepsilon_{xx} dS$$
$$= \int -yE_j(y)\left[\frac{du_j}{dx} - y\frac{d\theta_j}{dx}\right] dS \tag{C-3}$$

leading to:

$$M_j = -\left(\int E_j(y) y dS\right)\frac{du_j}{dx} + \left(\int E_j(y) y^2 dS\right)\frac{d\theta_j}{dx}$$
$$= -B_j\frac{du_j}{dx} + D_j\frac{d\theta_j}{dx} \tag{C-4}$$

To take into account for the nonlinear behavior of adherends, the iterative Newton-Raphson procedure associated with the secant stiffness matrix is used, which is detailed in (Lélias et al., 2015). The secant Young's modulus of adherends is then updated following the behavior law identified in Table 4. As a result the stiffness parameters A_j, B_j and D_j are updated consequently. In particular, when the isotropic adherends begin to plasticize, the coupling membrane-bending stiffness B_j could become different from zero.

References

Alfredsson, K.S., Biel, A., Leffler, K., 2003. An experimental method to determine the complete stress-deformation relation for a structural adhesive layer loaded in shear. Proceeding to 9th International Conference on The Mechanical Behavior of Materials.

Alfredsson, K.S., 2004. On the instantaneous energy release rate of the end notched flexure adhesive joint specimen. Int. J. Solids Struct 41, 4787–4807.

Allix, O., Ladevèze, P., 1996. Damage mechanics of interfacial media: Basic aspects, identification and application to delamination. In: Allen, D., Voyiadjis, G. (Eds.),

Damage and Interfacial Debonding in Composites, Studies in Applied Mechanics, 44. Elsevier, pp. 167–188.
Anderson, T., Stigh, U., 2004. The stress-elongation relation for an adhesive loaded in peel using equilibrium of energetic forces. Int. J. Solids Struct. 41, 413–434.
Andrews, H.C., Patterson, C.L., 1976. Singular value decomposition and digital iamge processing. IEEE Trans. ASSP 24, 26–53.
Azari, S., Eskandarian, M., Papini, M., Schroeder, J.A., Spelt, J.K., 2009. Fracture load predictions and measurements for toughened epoxy adhesive joints. Eng. Fract. Mech. 76, 2039–2055.
Bartczak, Z., Geleski, A., 2010. Plasticity of semicrystalline polymers. Macromol. Symp. 294 (1), 67–90.
Campilho, R.D.S.G., Banea, M.D., Neto, J.A.B.P., Da Silva, L.F.M., 2013. Modelling adhesive joints with cohesive zone models: Effects of the cohesive law shape of the adhesive layer. Int. J. Adhes. Adhes. 44, 48–56.
Clarke, J.L., 2003. Structural Design of Polymer Composites: Eurocomp Design Code and Background Document, 0203475135. CRCpress ISBN 9780203475133.
Cui, H., Koussios, S., Li, Y., Beukers, A., 2014. Constitutive law of adhesive layer measured with mixed-mode bending test. Eng. Fract. Mech. 127, 235–251.
Da Silva, L.F.M., Campilho, R.D.S.G., 2012. Advances in Numerical Modeling of Adhesive Joints. Springer Briefs in Computational Mechanics doi:10.1007/978-642-23608_1.
De Moura, M.F.S.F., Campilho, R.D.S.G., Goncalves, J.P.M., 2009. Mixed-mode cohesive damage model applied to the simulation of the mechanical behavior of laminated composite adhesive joints. J. Adhes. Sci. Technol. 23 (Issue 10-11), 1477–1491.
Fraisse, P., Schmit, F., 1993. Use of J-integral as fracture parameter in simplified analysis of bonded joints. Int. J. Fract 63, 59–73.
Goland, M., Reissner, E., 1944. The stresses in cemented joints. J. Appl. Mech. 11, A17–A27.
Gowrishankar, S., Mei, H., Liechti, K.M., Huang, R., 2012. A comparison of direct and iterative methods for determining traction-separation relations. Int. J. Fract. 177, 109–128.
Goustanios, S., Sørensen, B.F., 2012. Path dependence of truss-like mixed mode cohesive laws. Eng. Fract. Mech. 91, 117–132.
Gustafson, P.A., Bizard, A., Waas., M., 2006. A macroscopic joint finite element for a symmetric double lap joint. In: Proceedings of the American Society of Composites 21st Annual Technical Conferences, No. 24. American Society of Composites.
Gustafson, P.A., Waas, A.M., 2007. A macroscopic finite element for a symmetric double lap joint subjected to mechanical and thermal loading. In: 48th AIAA/ASME/ASCE/AHS/ASC Structures, Structural Dynamics, and Materials Conference. Honolulu, Hawaii, pp. 23–26. April 2007.
Gustafson, P.A., 2018. Analytical and Experimental Methods for Adhesively Bonded Joints Subjected to High Temperatures PhD Thesis. University of Michigan, Michigan.
Gustafson, P.A., Waas, A.M., 2009. A bonded joint finite element for a symmetric double lap joint subjected to mechanical and thermal loads. Int. J. Numer. Meth. Eng. 79 (1), 94–126.
Hart-Smith, L.J., 1973. Adhesive Bonded Single Lap joints. Douglas Aircraft Company, Long Beach, California NASA Technical Report, CR-112236.
Hart-Smith, L.J., 1980. Adhesive Bonding of Aircraft Primary Structures. SAE Technical Paper.
Högberg, J.L., 2006. Mixed-mode testing of adhesive layer. Proceeding to 27th International Symposium on Materials Science, Polymer Composite Materials for Wind Power Turbines.
Högberg, J.L., Stigh, U., 2006. Specimen proposals for mixed-mode testing of adhesive layer. Eng. Fract. Mech. 73, 2541–2556.
Jumel, J., Budzik, M.K., Ben Salem, N., Shanahan, M.E.R., 2013. Instrumented end notched flexure – crack propagation and process zone monitoring. Part I: modelling and analysis. Int. J. Adhes. Adhes. 50, 297–309 N 2.
Khoramishad, H., Crocombe, A.D., Katnam, K.B., Ashcroft, I.A., 2010. A generalized damage model for constant amplitude fatigue loading of adhesively bonded joints. Int. J. Adhes. Adhes. 30, 513–521.
Khoramishad, H., Crocombe, A.D., Katnam, K.B., Ashcroft, I.A., 2011. Fatigue damage modeling of adhesively bonded joints under variable amplitude loading using cohesive zone model. Eng. Fract. Mech. 78, 3212–3225.
Kelly, G., 2006. Quasi-static strength and fatigue life of hybrid (bonded/bolted) composite single-lap joints. J. Compos. Struct. 72, 119–129.
Kenane, M., Benzeggagh, M.L., 1997. Mixed-mode delamination fracture toughness of unidirectional glass/epoxy composites under fatigue loading. Compos. Sci. Technol. 57, 597–605.
Leffler, K., Alfredsson, K.S., Stigh, U., 2007. Shear behavior of adhesive layers. Int. J. Solids Struct. 44, 530–545.
Lélias, G., Paroissien, E., Lachaud, F., Morlier, J., Schwartz, S., Gavoille, C., 2015. An extended semi-analytical formulation for fast and reliable mode I/II stress analysis of adhesively bonded joints. Int. J. Solids Struct. 62, 18–38.
Lélias, 2016. Adhesive bonded joints: Modeling Simulation and experimental characterization. PhD thesis, Universite de Toulouse. France.
Li, S., Thouless, M.D., Waas, A.M., Schroeder, Zavattieri, P.D., 2006. Mixedmode cohesive zone models for fracture of an adhesively bonded polymer matrix composite. Eng. Fract. Mech. 73, 64–78.
Luo, Q., Tong, L., 2009. Analytical solutions for nonlinear analysis of composite single-lap joints. Int. J. Adhes. Adhes. 29, 144–154.
Paroissien, E., 2006a. Contribution aux Assemblages Hybrides (Boulonnés/Collés) – Application aux Jonctions Aéronautiques. Université de Toulouse III (2006).
Paroissien, E., Sartor, M., Huet, J., Lachaud, F., 2006b. Hybrid (bolted/bonded) joints applied to aeronautic parts: analytical two-dimensional model of a hybrid (bolted/bonded) single-lap joint. In: 47th AIAA/ASME/ASCE/AHS/ASC Structures, Structural Dynamics, and Material Conference (47th SDM AIAA), 1–4 May 2006. Newport, pp. 2006–2268. (RI), paper AIAA.
Paroissien, E., Sartor, M., Huet, J., Lachaud, F., 2007. Analytical two-dimensional model of a hybrid (bolted/bonded) single-lap joint. J. Aircraft 44, 573–582.
Paroissien, E., Lachaud, F., Jacobs, T., 2013. A simplified stress analysis of bonded joints using macro-elements. In: Kumar, S., Mittal, K.L. (Eds.), Advances in Modeling and Design of Adhesively Bonded Bonded Systems. Wiley-Scrivener, Beverly, Massachusetts, pp. 93–146.
Paroissien, E., da Silva, L.F.M., Lachaud, F., 2018. Simplified stress analysis of functionally graded single-lap joints subjected to combined thermal and mechanical loads. Compos. Struct. 203, 85–100. doi:10.1016/j.compstruct.2018.07.015.
Reeder, J.R., Crews, J.R., 1990. Mixed-mode bending method for delamination testing. AIAAA J. 28, 1270–1276 N 7.
Rice, J.R., 1968. A path independent integral and the approximate analysis of strain concentration by notches and cracks. J. Appl. Mech 35, 379–386.
Stapleton, S.E.,P.A., Waas, A.M., 2007. Macroscopic finite element for a single lap joint. 50th AIAA/ASME/ASCE/AHS/ASC Structures, Structural Dynamics, and Materials Conference, 4–7 May 2009.
Stapleton, S.E.,P.A., Waas, A.M., Bednarcyk, B.A., 2010. Modelling progressive failure of bonded joints using a single joint finite element. 51st AIAA/ASME/ASCE/AHS/ASC Structures, Structural Dynamics, and Materials Conference, 12-15 April 2010.
Stapleton, S.E., 2012. The Analysis of Adhesively Bonded Advanced Composite Joints Using Joint Finite elements PhD Thesis. University of Michigan, Michigan.
Stapleton, S.E., Waas, A.M., Arnold, S.M., 2012. Functionally graded adhesive joints. Int. J. Adhes. Adhes. 35, 36–49.
Stapleton, S.E., Weimer, J., Spengler, J., 2017. Design of functionally graded joints using a polyurethane-based adhesive with varying amounts of acrylate. Int. J. Adhes. Adhes. 76, 38–46.
Tsai, M.Y., Oplinger, D.W., Morton, J., 1998. Improved theoretical solutions for adhesive lap joints. Int. J. Solids Struct. 35, 1163–1185.
Turon, A., Camanho, P.P., Costa, J., Renart, J., 2010. Accurate simulation of delamination growth under mixed-mode loading using cohesive elements: definition of interlaminar strengths and elastic stiffness. Compos. Struct. 92, 1857–1864.
Valoroso, N., Champaney, L., 2004. A damage model for simulating decohesion in adhesively bonded assemblies. Proceeding to European Congress on Computational Methods in Applied Sciences and Engineering.
Weissgraeber, P., Stein, N., Becker, W., 2014. A general sandwich type model for adhesive joints with composite adherends. Int. J. Adhes. Adhes. 55, 56–63.
Wu, C., Gowrishankar, S., Huang, R., Liechit, K.M., 2013. On determining mixed-mode traction-seperation relations for interfaces. Int. J. Fract. 202, 1–19.